

1 LEVERAGING MULTI-MESSENGER ASTROPHYSICS FOR DARK MATTER SEARCHES

By

Daniel Nicholas Salazar-Gallegos

A DISSERTATION

Submitted to
Michigan State University
in partial fulfillment of the requirements
for the degree of

Physics—Doctor of Philosophy
Computational Mathematics in Science and Engineering—Dual Major

Today

ABSTRACT

3 I did Dark Matter with HAWC and IceCube. I also used Graph Neural Networks

⁴ Copyright by

⁵ DANIEL NICHOLAS SALAZAR-GALLEGOS

⁶ Today

ACKNOWLEDGMENTS

8 I love my friends. Thanks to everyone that helped me figure this out. Amazing thanks to the people
9 at LANL who supported me. Eames, etc Dinner Parties Jenny and her child Kaydince Kirsten, Pat,
10 Andrea Family. You're so far but so critical to my formation. Unconditional love. Roommate

TABLE OF CONTENTS

12	LIST OF TABLES	vii
13	LIST OF FIGURES	viii
14	LIST OF ABBREVIATIONS	xiii
15	CHAPTER 1 INTRODUCTION	1
16	CHAPTER 2 DARK MATTER IN THE COSMOS	2
17	2.1 Introduction	2
18	2.2 Dark Matter Basics	3
19	2.3 Evidence for Dark Matter	4
20	2.4 Searching for Dark Matter: Particle DM	11
21	2.5 Sources for Indirect Dark Matter Searches	16
22	2.6 Multi-Messenger Dark Matter	18
23	CHAPTER 3 MULTIMESSENGER ASTROPHYSICS: DETECTING HIGH EN-	
24	ERGY NEUTRAL MESSENGERS	21
25	3.1 Introduction	21
26	3.2 Charged Particles in a Medium	21
27	3.3 Photons (γ)	22
28	3.4 Neutrinos (ν)	22
29	3.5 Opportunities to Combine for Dark Matter	22
30	CHAPTER 4 HIGH ALTITUDE WATER CHERENKOV (HAWC) OBSERVATORY .	24
31	4.1 The Detector	24
32	4.2 Events Reconstruction and Data Acquisition	24
33	4.3 Remote Monitoring	24
34	CHAPTER 5 ICECUBE NEUTRINO OBSERVATORY	25
35	5.1 The Detector	25
36	5.2 Events Reconstruction and Data Acquisition	25
37	5.3 Northern Test Site	25
38	CHAPTER 6 COMPUTATIONAL TECHNIQUES IN PARTICLE ASTROPHYSICS .	26
39	6.1 Neural Networks for Gamma/Hadron Separation	26
40	6.2 Parallel Computing for Dark Matter Analyses	26
41	CHAPTER 7 GLORY DUCK: MULTI-WAVELENGTH SEARCH FOR DARK MATT-	
42	TER ANNIHILATION TOWARDS DWARF SPHEROIDAL GALAX-	
43	IES	27
44	7.1 Introduction	27
45	7.2 Dataset and Background	29
46	7.3 Analysis	30

47	7.4 HAWC Results	38
48	7.5 Glory Duck Combined Results	39
49	7.6 HAWC Systematics	43
50	7.7 <i>J</i> -factor distributions	48
51	7.8 Discussion and Conclusions	53
52	CHAPTER 8 NU DUCK	57
53	CHAPTER 9 MULTITHREADING HAWC ANALYSES FOR DARK MATTER	
54	SEARCHES	58
55	BIBLIOGRAPHY	59

LIST OF TABLES

<p>57 Table 7.1 Summary of the relevant properties of the dSphs used in the present work. 58 Column 1 lists the dSphs. Columns 2 and 3 present their heliocentric distance 59 and galactic coordinates, respectively. Columns 4 and 5 report the J-factors of 60 each source given from the \mathcal{GS} and \mathcal{B} independent studies and their estimated 61 $\pm 1\sigma$ uncertainties. The values $\log_{10} J$ (\mathcal{GS} set) [44] correspond to the mean 62 J-factor values for a source extension truncated at the outermost observed star. 63 The values $\log_{10} J$ (\mathcal{B} set) [46] are provided for a source extension at the tidal 64 radius of each dSph. Bolded sources are within HAWC's field of view and 65 provided to the Glory Duck analysis.</p>	<p style="margin: 0;">. 35</p>
<p>66 Table 7.2 Summary of dSph observations by each experiment used in this work. A 67 ‘-’ indicates the experiment did not observe the dSph for this study. For 68 Fermi-LAT, the exposure at 1 GeV is given. For HAWC, $\Delta\theta$ is the absolute 69 difference between the source declination and HAWC latitude. HAWC is more 70 sensitive to sources with smaller $\Delta\theta$. For IACTs, we show the zenith angle 71 range, the total exposure, the energy range, the angular radius θ of the signal or 72 ON region, the ratio of exposures between the background-control (OFF) and 73 signal (ON) regions (τ), and the significance of gamma-ray excess in standard 74 deviations, σ.</p>	<p style="margin: 0;">. 36</p>
<p>75 Proof I know how to include</p>	

LIST OF FIGURES

77	Figure 2.1	Rotation curve fit to NGC 6503 from [7]. Dashed line is the contribution 78 from visible matter. Dotted curves are from gas. Dash-dot curves are from 79 dark matter (DM). Solid line is the composite contribution from all matter 80 and DM sources. Data are indicated with bold dots with error bars. Data 81 agree strongly with a matter + DM composite prediction.	5
82	Figure 2.2	Light from distant galaxy is bent in unique ways depending on the distribution 83 of mass between the galaxy and Earth. Yellow dashed lines indicate where 84 the light would have gone if the matter were not present [8].	7
85	Figure 2.3	(left) Optical image of galactic cluster 1E0657-558. (right) X-ray image of the 86 cluster with redder meaning hotter and higher baryon density. (both) Green 87 contours are reconstruction of gravity contours from weak lensing. White 88 rings are the best fit mass maxima at 68.3%, 95.5%, and 99.7% confidence. 89 The matter maxima of the clusters are clearly separated from x-ray maxima. [9]	8
90	Figure 2.4	Plank CMB sky. Sky map features small variations in temperature in primor- 91 dial light. These anisotropies are used to make inferences about the universe's 92 energy budget and developmental history. [10]	9
93	Figure 2.5	Observed Cosmic Microwave Background power spectrum as a function of 94 multipole moment from Plank [10]. Blue line is best fit model from Λ CDM. 95 Red points and lines are data and error, respectively.	10
96	Figure 2.6	Predicted power spectra of CMB for different $\Omega_m h^2$ values for fixed baryon 97 density from [11]. (left) Low $\Omega_m h^2$ increases the prominence of first and 98 second peaks. (middle) $\Omega_m h^2$ is most similar to the observed power spectrum. 99 The second and third peaks are similar in height. (right) $\Omega_m h^2$ is large which 100 suppresses the first peak and raises the prominence of the third peak.	10
101	Figure 2.7	The Standard Model (SM) of particle physics. Figure taken from http://www.quantumdiaries.org/2014/03/14/the-standard-model-a-beautiful-but-flawed-theory/	12
104	Figure 2.8	Simplified Feynman diagram demonstrating with different ways DM can 105 interact with SM particles. The 'X's refer to the DM particles whereas the 106 SM refer to fundamental particles in the SM. The large circle in the center 107 indicates the vertex of interaction and is purposely left vague. The colored 108 arrows refer to different directions of time as well as their respective labels. 109 The arrows indicate the initial and final state of the DM -SM interaction in time.	13

110	Figure 2.9 A single jet event in ATLAS detector from 2017 [16]. Jet momentum was 111 observed to be 1.9 TeV. Missing transverse momentum was observed to be 112 1.9 TeV compared to the initial transverse momentum of the event was 0. 113 Implied MET is traced by a red dashed line in event display.	14
114	Figure 2.10 More detailed pseudo-Feynman diagram of particle cascade from dark matter 115 annihilation into 2 quarks. The quarks hadronize and down to stable particles 116 like γ or the anti-proton (p^-). Diagram pulled from ICRC 2021 presentation 117 on DM annihilation search [17].	15
118	Figure 2.11 Dark Matter (DM) decay spectrum for $b\bar{b}$ initial state and γ final state. Redder 119 spectra are for larger DM masses. Bluer spectra are light DM masses. x is a 120 unitless factor defined as the ratio of the mass of DM, m_χ , and the final state 121 particle energy E_γ . Figure from [19].	17
122	Figure 2.12 Different dark matter density profiles compared. Some models produce ex- 123 ceptionally large densities at small r [20].	18
124	Figure 2.13 The Milky Way Galaxy in photons (γ) and neutrinos (ν) [22]. The Galactic 125 center is at $l=0^\circ$ and is the brightest region in all panels. (top) An Optical 126 color image of the Milky Way galaxy seen from Earth. Clouds of gas and dust 127 obscure some light from stars. (2nd down) Integrated flux of γ -rays observed 128 by the Fermi-LAT telescope [23]. (middle) Expected neutrino emission 129 that corresponds with Fermi-LAT observations. (2nd up) Expected neutrino 130 emission profile after considering detector systematics of IceCube. (bottom) 131 Observed neutrino emission from region of the galactic plane. Substantial 132 neutrino emission was detected.	19
133	Figure 2.14 Dark Matter annihilation spectra for different final state particle and standard 134 model annihilation channels [24]. Photons (red), e^\pm (green), \bar{p} (blue), ν (black).	20
135	Figure 3.1 TODO: Show a nuclear reactor with cherenkov radiation[NEEDS A SOURCE][FACT 136 CHECK THIS]	22
137	Figure 3.2 TODO: absorption spectrum of liquid and solid water[NEEDS A SOURCE][FACT 138 CHECK THIS]	23

139	Figure 7.1 [NEEDS A SOURCE] Sensitivities of five gamma-ray experiments compared 140 to percentages of the Crab nebula's emission and dark matter annihilation. 141 Solid lines present estimated sensitivities to power law spectra [FACT CHECK 142 THIS]for each experiment. Green lines are Fermi-LAT sensitivities where 143 lighter green is the sensitivity to the galactic center and light green is its sen- 144 sitivity to higher declinations. Orange, red, and purple solid lines represent 145 the MAGIC, HESS, and VERITAS 50 hour sensitivities respectively. The 146 maroon and brown lines are the HAWC 1 year and 5 year sensitivities. Across 147 four decades of gamma-ray energy, these experiments have similar sensitiv- 148 ities on the order 10^{-12} erg cm $^{-2}$ s $^{-1}$. The dotted lines are estimated dark 149 matter fluxes assuming DM annihilating to bottom quarks (red), tau leptons 150 (blue), and W bosons (green). Faded grey lines outline percentage flux of the 151 Crab nebula.	27
152	Figure 7.2 Effect of Electro-Weak (EW) corrections on expected DM annihilation spec- 153 trum for $\chi\chi \rightarrow W^-W^+$. Solid lines are spectral models that consider EW 154 corrections. Dash-dot lines are spectral models without EW corrections. Red 155 lines are models for $M_\chi = 1$ TeV. Blue lines represent models for $M_\chi = 100$ 156 TeV. All models are sourced from the PPPC4DMID [43].	32
157	Figure 7.3 $\frac{dJ}{d\Omega}$ maps for Segue1 (top) and Coma Berenices (bottom). Origin is centered 158 on the specific dwarf spheroidal galaxies (dSph). X and Y axes are the 159 angular separation from the center of the dwarf. Plots of the remaining 11 160 dSph HAWC studied are linked in Section 7.2.2.	33
161	Figure 7.4 Illustration of the combination technique showing a comparison between 162 $-2 \ln \lambda$ provided by four instruments (colored lines) from the observation 163 of the same dSph without any J nuisance and their sum, <i>i.e.</i> the result- 164 ing combined likelihood (thin black line). According to the test statistics 165 of Equation (7.10), the intersection of the likelihood profiles with the line 166 $-2 \ln \lambda = 2.71$ indicates the 95% C.L. upper limit on $\langle \sigma v \rangle$. The combined 167 likelihood (thin black line) shows a smaller value of upper limit on $\langle \sigma v \rangle$ 168 than those derived by individual instruments. We also show the uncertainties 169 on the J -factor affects the combined likelihood and degrade the upper limit 170 on $\langle \sigma v \rangle$ (thick black line). All likelihood profiles are normalized so that the 171 global minimum $\widehat{\langle \sigma v \rangle}$ is 0. We note that each profile depends on the observa- 172 tional conditions in which a target object was observed. The sensitivity of a 173 given instrument can be degraded and the upper limits less constraining if the 174 observations are performed in non optimal conditions such as a high zenith 175 angle or a short exposure time.	39
176	Figure 7.5 HAWC upper limits at 95% confidence level on $\langle \sigma v \rangle$ versus DM mass for 177 seven annihilation channels, using the set of J -factors from Ref. [47] The 178 solid line represents the observed combined limit. Dashed lines represent 179 limits from individual dSphs.	40

180	Figure 7.6 HAWC Brazil bands at 95% confidence level on $\langle\sigma v\rangle$ versus DM mass for	41
181	seven annihilation channels with J -factors from \mathcal{GS} [47]. The solid line	
182	represents the combined limit from 13 dSphs. The dashed line is the expected	
183	limit. The green band is the 68% containment. The yellow band is the 95%	
184	containment.	
185	Figure 7.7 Upper limits at 95% confidence level on $\langle\sigma v\rangle$ in function of the DM mass for	44
186	eight annihilation channels, using the set of J factors from Ref. [47] (\mathcal{GS} set	
187	in Table 7.1). The black solid line represents the observed combined limit,	
188	the black dashed line is the median of the null hypothesis corresponding	
189	to the expected limit, while the green and yellow bands show the 68% and	
190	95% containment bands. Combined upper limits for each individual detector	
191	are also indicated as solid, colored lines. The value of the thermal relic	
192	cross-section in function of the DM mass is given as the red dotted-dashed	
193	line [52].	
194	Figure 7.8 Same as Fig. 7.7, using the set of J factors from Ref. [46, 51] (\mathcal{B} set in Table 7.1).	45
195	Figure 7.9 Comparisons of the combined limits at 95% confidence level for each of the	46
196	eight annihilation channels when using the J factors from Ref. [47] (\mathcal{GS} set in	
197	Table 7.1), plain lines, and the J factor from Ref. [46, 51] (\mathcal{B} set in Table 7.1),	
198	dashed lines. The cross-section given by the thermal relic is also indicated [52].	
199	Figure 7.10 Comparisons of the combined limits at 95% confidence level for a point source	47
200	analysis and extended source using [47] \mathcal{GS} J-factor distributions and PPPC	
201	[43] annihilation spectra. Shown are the limits for Segue1 which will have	
202	the most significant impact on the combined limit. 6 of the 7 DM annihilation	
203	channels are shown. Solid lines are extended source studies. Dashed lines	
204	are point source studies. Overall, the extended source analysis improves the	
205	limit by a factor of 2.	
206	Figure 7.11 Same as Fig. 7.10 on Coma Berenices. This dSph also contributes signifi-	48
207	cantly to the limit. The limits are identical in this case.	
208	Figure 7.12 Comparison of combined limits when correcting for HAWC's pointing sys-	49
209	tematic. All DM annihilation channels are shown. The solid black line is the	
210	ratio between published limit to the declination corrected limit. The blue solid	
211	line or "Combined_og" represented the limits computed for Glory Duck. The	
212	solid orange line or "Combined_ad" represented the limits computed after	
213	correcting for the pointing systematic.	
214	Figure 7.13 Differential map of dJ/Ω from model built in Section 7.7.1 and profiles	51
215	provided directly from authors. (Top) Differential from Segue1. (bottom)	
216	Differential from Coma Berenices. Note that their scales are not the same.	
217	Segue1 shows the deepest discrepancies which is congruent with its large	
218	uncertainties. Both models show anuli where unique models become apparent.	

219	Figure 7.14 HAWC limits for Coma Berenices (top) and Segue1 (bottom) for two different 220 map sets. Blue lines are limits calculated on maps with poor model repre- 221 sentation. Orange lines are limits calculated on spatial profiles provided by 222 the authors of [44]. Black line is the ratio of the poor spatial model limits to 223 the corrected spatial models. The left y-axis measures $\langle \sigma v \rangle$ for the blue and 224 orange lines. The right y-axis measures the ratio and is unitless.	52
225	Figure 7.15 Comparisons between the J -factors versus the angular radius for the com- 226 putation of J factors from Ref. [47] (\mathcal{GS} set in Table 7.1) in blue and for 227 the computation from Ref. [46, 51] (\mathcal{B} set in Tab. 7.1) in orange. The solid 228 lines represent the central value of the J -factors while the shaded regions 229 correspond to the 1σ standard deviation.	54
230	Figure 7.16 Comparisons between the J -factors versus the angular radius for the computa- 231 tion of J factors from Ref. [47] (\mathcal{GS} set in Tab. 7.1) in blue and for the 232 computation from Ref. [46, 51] (\mathcal{B} set in Tab. 7.1) in orange. The solid 233 lines represent the central value of the J -factors while the shaded regions 234 correspond to the 1σ standard deviation.	55

LIST OF ABBREVIATIONS

- 236 **MSU** Michigan State University
237 **LANL** Los Alamos National Laboratory
238 **DM** Dark Matter
239 **SM** Standard Model
240 **HAWC** High Altitude Water Cherenkov Observatory

241

CHAPTER 1

INTRODUCTION

242 Is the text not rendering right? Ah ok it knows im basically drafting the doc still

CHAPTER 2

243

DARK MATTER IN THE COSMOS

244 2.1 Introduction

245 The dark matter problem can be summarized in part by the following thought experiment.

246 Let us say you are the teacher for an elementary school classroom. You take them on a field
247 trip to your local science museum and among the exhibits is one for mass and weight. The exhibit
248 has a gigantic scale, and you come up with a fun problem for your class.

249 You ask your class, "What is the total weight of the classroom? Give your best estimation to
250 me in 30 minutes, and then we'll check your guess on the scale. If your guess is within 10% of the
251 right answer, we will stop for ice cream on the way back."

252 The students are ecstatic to hear this, and they get to work. The solution is some variation of
253 the following strategy. The students should give each other their weight or best guess if they do
254 not know. Then, all they must do is add each student's weight and get a grand total for the class.
255 The measurement on the giant scale should show the true weight of the class. When comparing
256 the measured weight to your estimation, multiply the measurement by 1.0 ± 0.1 to get the $\pm 10\%$
257 tolerances for your estimation.

258 Two of your students, Sandra and Mario, return to you with a solution.

259 They say, "We weren't sure of everyone's weight. We used 65 lbs. for the people we didn't
260 know and added everyone who does know. There are 30 of us, and we got 2,000 lbs.! That's a ton!"

261 You estimated 1,900 lbs. assuming the average weight of a student in your class was 60 lbs.
262 So, you are pleased with Sandra's and Mario's answer. You instruct your students to all gather on
263 the giant scale and read off the weight together. To all your surprise, the scale reads *10,000 lbs.*!
264 10,000 is significantly more than a 10% error from 2,000. In fact, it is approximately 5 times more
265 massive than either your or your students' estimates. You think to yourself and conclude there
266 must be something wrong with the scale. You ask an employee to check the scale and verify it is
267 well calibrated. They confirm that the scale is in working order. You weigh a couple of students
268 individually to assess that the scale is well calibrated. Sandra weighs 59 lbs., and Mario weighs

269 62 lbs., typical weights for their age. You then weigh each student individually and see that their
270 weights individually do not deviate greatly from 60 lbs. So, where does all the extra weight come
271 from?

272 This thought experiment serves as an analogy to the Dark Matter problem. The important
273 substitution to make however is to replace the students with stars and the classroom with a galaxy,
274 say the Milky Way. Individually the mass of stars is well measured and defined with the Sun as our
275 nearest test case. However, when we set out to measure the mass of a collection of stars as large as
276 galaxies, our well-motivated estimation is wildly incorrect. There simply is no way to account for
277 this discrepancy except without some unseen, or dark, contribution to mass and matter in galaxies.
278 I set out in my thesis to narrow the possibilities of what this Dark Matter could be.

279 This chapter is organized like the following... **TODO: Text should look like ... Chapter x has**
280 **blah blah blah.**

281 **2.2 Dark Matter Basics**

282 Presently, a more compelling theory of cosmology that includes Dark Matter (DM) in order
283 to explain a variety of observations is Λ Cold Dark Matter, or Λ CDM. I present the evidence
284 supporting Λ CDM in Section 2.3 yet discuss the conclusions of the Λ CDM model here. According
285 to Λ CDM fit to observations on the Cosmic Microwave Background (CMB), DM is 26.8% of the
286 universe's current energy budget. Baryonic matter, stuff like atoms, gas, and stars, contributes to
287 4.9% of the universe's current energy budget [1, 2, 3].

288 DM is dark; it does not interact readily with light at any wavelength. DM also does not interact
289 noticeably with the other standard model forces (Strong and Weak) at a rate that is readily observed
290 [3]. DM is cold, which is to say that the average velocity of DM is below relativistic speeds [1].
291 'Hot' DM would not likely manifest the dense structures we observe like galaxies, and instead
292 would produce much more diffuse galaxies than what is observed [3, 1]. DM is old; it played a
293 critical role in the formation of the universe and the structures within it [1, 2].

294 Observations of DM have so far been only gravitational. The parameter space available to what
295 DM could be therefore is extremely broad. The broad DM parameter space is iteratively tested in

296 DM searches by supposing a hypothesis that has not yet been ruled out and performing observations
297 to test them. When the observations yield a null result, the parameter space is constrained further.
298 I present some approaches for DM searches in Section 2.4.

299 **2.3 Evidence for Dark Matter**

300 Dark Matter (DM) has been a looming problem in physics for almost 100 years. Anomalies
301 have been observed by astrophysicists in galactic dynamics as early as 1933 when Fritz Zwicky
302 noticed unusually large velocity dispersion in the Coma cluster. Zwicky's measurement was the
303 first recorded to use the Virial theorem to measure the mass fraction of visible and invisible matter
304 in celestial bodies [4]. From Zwicky in [5], "*If this would be confirmed, we would get the surprising*
305 *result that dark matter is present in much greater amount than luminous matter.*" Zwicky's and
306 others' observation did not instigate a crisis in astrophysics because the measurements did not
307 entirely conflict with their understanding of galaxies [4]. In 1978, Rubin, Ford, and Norbert
308 measured rotation curves for ten spiral galaxies [6]. Rubin et al.'s 1978 publication presented a
309 major challenge to the conventional understanding of galaxies that could no longer be dismissed by
310 measurement uncertainties. Evidence has been mounting ever since for this exotic form of matter.
311 The following subsections provide three compelling pieces of evidence in support of the existence
312 of DM.

313 **2.3.1 First Clues: Stellar Velocities**

314 Zwicky, and later Rubin, measured the stellar velocities of various galaxies to estimate their
315 virial mass. The Virial Theorem upon which these observations are interpreted is written as

$$2T + V = 0. \quad (2.1)$$

316 Where T is the kinetic energy and V is the potential energy in a self-gravitating system. The
317 classical Newton's law of gravity from stars and gas was used for gravitational potential modeled in
318 the observed galaxies:

$$V = -\frac{1}{2} \sum_i \sum_{j \neq i} \frac{m_i m_j}{r_{ij}}. \quad (2.2)$$

319 Zwicky et al. measured just the velocities of stars apparent in optical wavelengths [5]. Rubin et al.
 320 added by measuring the velocity of the hydrogen gas via the 21 cm emission line of Hydrogen [6].
 321 The velocities of the stars and gas are used to infer the total mass of galaxies and galaxy clusters
 322 via Equation (2.1). An inferred mass is obtained from the luminosity of the selected sources. The
 323 two inferences are compared to each other as a luminosity to mass ratio which typically yielded [1]

$$\frac{M}{L} \sim 400 \frac{M_{\odot}}{L_{\odot}} \quad (2.3)$$

324 M_{\odot} and L_{\odot} referring to stellar mass and stellar luminosity, respectively. These ratios clearly indicate
 325 a discrepancy in apparent light and mass from stars and gas and their velocities.

326 Rubin et al. [6] demonstrated that the discrepancy was unlikely to be an underestimation of
 327 the mass of the stars and gas. The inferred "dark" mass was up to 5 times more than the luminous
 328 mass. This dark mass also needed to extend well beyond the extent of the luminous matter.

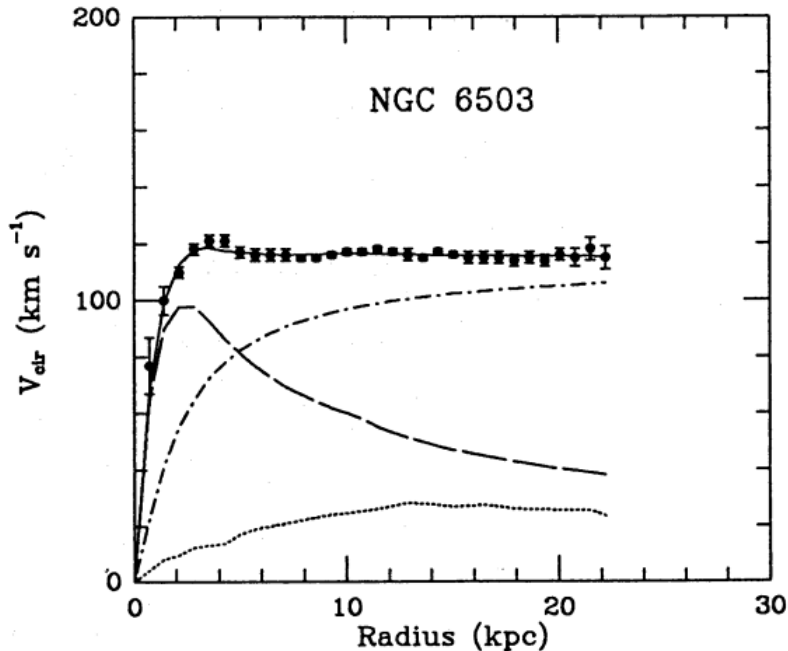


Figure 2.1 Rotation curve fit to NGC 6503 from [7]. Dashed line is the contribution from visible matter. Dotted curves are from gas. Dash-dot curves are from dark matter (DM). Solid line is the composite contribution from all matter and DM sources. Data are indicated with bold dots with error bars. Data agree strongly with a matter + DM composite prediction.

329 Figure 2.1 features one of many rotation curves plotted from the stellar velocities within galaxies.

330 The measured rotation curves mostly feature a flattening of velocities at higher radius which is not
331 expected if the gravity was only coming from gas and luminous matter. The extension of the
332 flat velocity region also indicates that the DM is distributed far from the center of the galaxy.
333 Modern velocity measurements include significantly larger objects, galactic clusters, and smaller
334 objects, dwarf galaxies. Yet, measurements along this regime are leveraging the Virial theorem
335 with Newtonian potential energies. We know Newtonian gravity is not a comprehensive description
336 of gravity. New observational techniques have been developed since 1978, and those are discussed
337 in the following sections.

338 **2.3.2 Evidence for Dark Matter: Gravitational Lensing**

339 Modern evidence for dark matter comes from new avenues beyond stellar velocities. Grav-
340 itational lensing from DM is a new channel from general relativity. General relativity predicts
341 aberrations in light caused by massive objects. In recent decades we have been able to measure the
342 lensing effects from compact objects and DM halos. Figure 2.2 shows how different massive ob-
343 jects change the final image of a faraway galaxy resulting from gravitational lensing. Gravitational
344 lensing developed our understanding of dark matter in two important ways.

345 Gravitational lensing provides additional compelling evidence for DM. The observation of two
346 merging galactic clusters in 2006, shown in Figure 2.3, provided a compelling argument for DM
347 outside the Standard Model. These clusters merged recently in astrophysical time scales. Galaxies
348 and star cluster have mostly passed by each other as the likelihood of their collision is low. Therefore,
349 these massive objects will mostly track the highest mass, dark and/or baryonic, density. Yet, the
350 intergalactic gas is responsible for the majority of the baryonic mass in the systems [4]. These gas
351 bodies will not phase through and will heat up as they collide together. The hot gas is located via
352 x-ray emission from the cluster. Two observations of the clusters were performed independently of
353 each other.

354 The first was the lensing of light around the galaxies due to their gravitational influences.
355 When celestial bodies are large enough, the gravity they exert bends space and time itself. The
356 warped space-time lenses light and will deflect in an analogous way to how glass lenses will bend

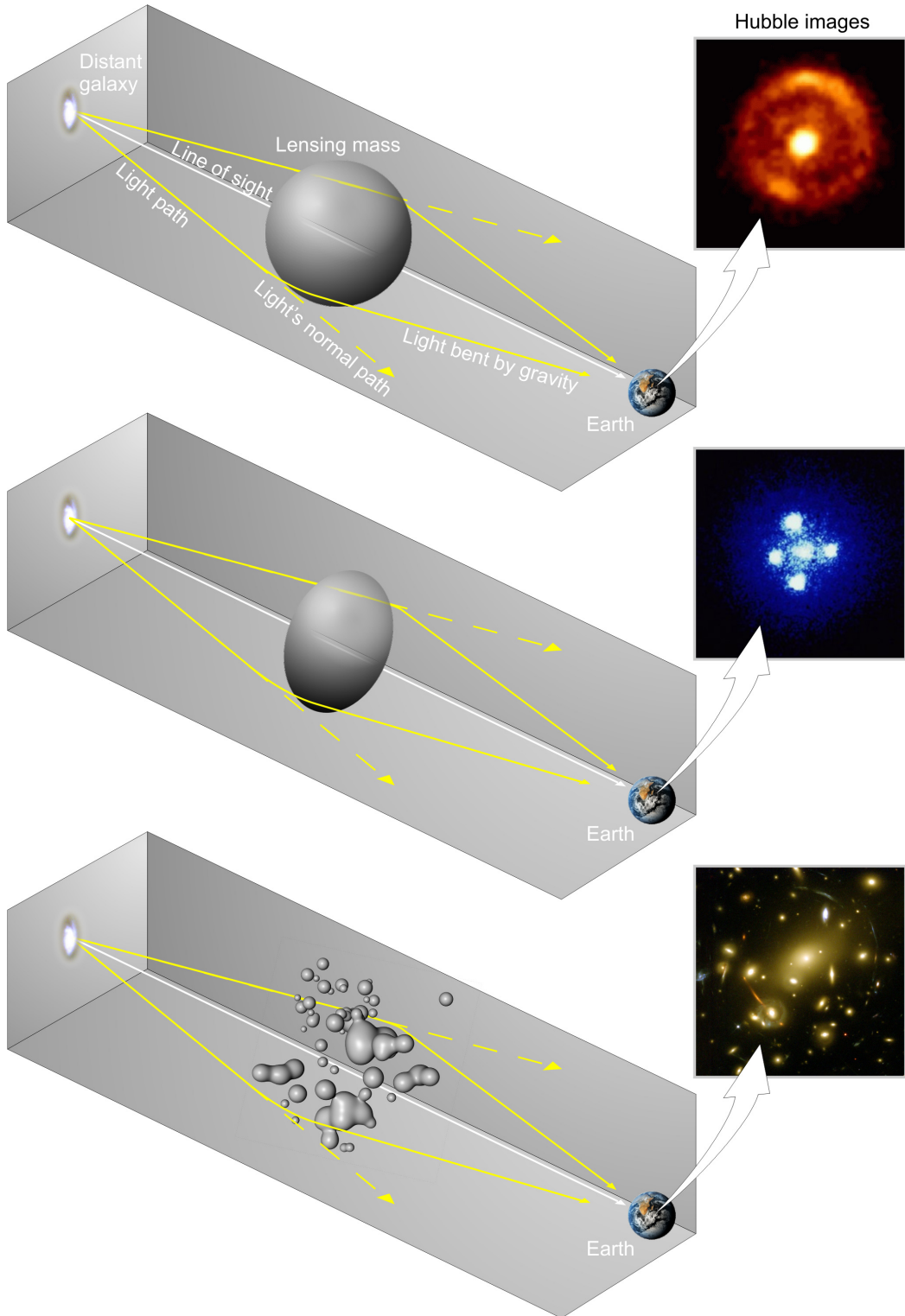


Figure 2.2 Light from distant galaxy is bent in unique ways depending on the distribution of mass between the galaxy and Earth. Yellow dashed lines indicate where the light would have gone if the matter were not present [8].

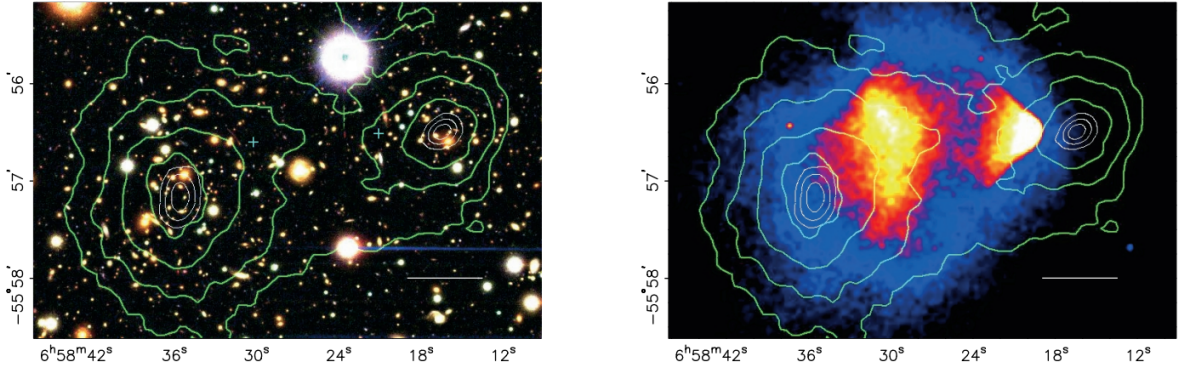


Figure 2.3 (left) Optical image of galactic cluster 1E0657-558. (right) X-ray image of the cluster with redder meaning hotter and higher baryon density. (both) Green contours are reconstruction of gravity contours from weak lensing. White rings are the best fit mass maxima at 68.3%, 95.5%, and 99.7% confidence. The matter maxima of the clusters are clearly separated from x-ray maxima. [9]

357 light, see Figure 2.2. With a sufficient understanding of light sources behind a massive object, we
 358 can reconstruct the contours of the gravitational lenses. The gradient of the contours shown in
 359 Figure 2.3 then indicates how dense the matter is and where it is.

360 The x-ray emission can then be observed from the clusters. Since these galaxies are mostly gas
 361 and are merging, then the gas should be getting hotter. If they are merging, the x-ray emissions
 362 should be the strongest where the gas is mostly moving through each other. Hence, X-ray emission
 363 maps out where the gas is in the merging galaxy cluster.

364 The lensing and x-ray observations were done on the Bullet cluster featured on Figure 2.3.
 365 The x-ray emissions do not align with the gravitational contours from lensing. The incongruence
 366 in mass density and baryon density suggests that there is a lot of matter somewhere that does
 367 not interact with light. Moreover, this dark matter cannot be baryonic [9]. The Bullet Cluster
 368 measurement did not really tell us what DM is exactly, but it did give the clue that DM also does
 369 not interact with itself very strongly. If DM did interact strongly with itself, then it would have been
 370 more aligned with the x-ray emission [9]. There have been follow-up studies of galaxy clusters with
 371 similar results. The Bullet Cluster and others like it provide a persuasive case against something
 372 possibly amiss in our gravitational theories.

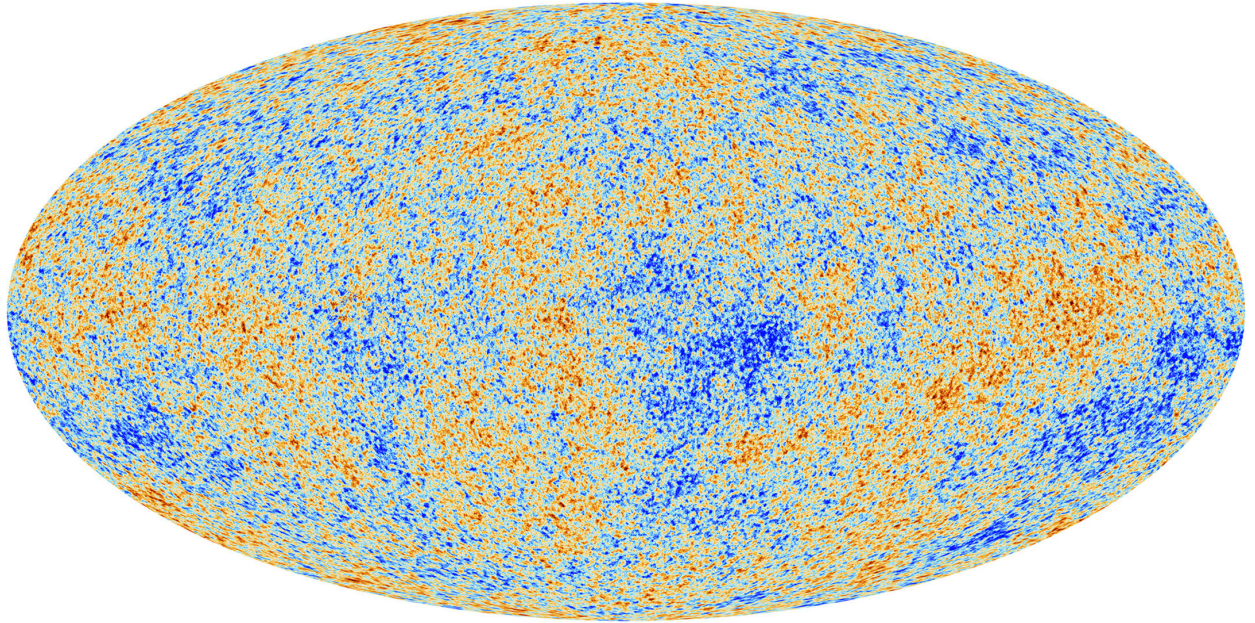


Figure 2.4 Plank CMB sky. Sky map features small variations in temperature in primordial light. These anisotropies are used to make inferences about the universe’s energy budget and developmental history. [10]

373 **2.3.3 Evidence for Dark Matter: Cosmic Microwave Background**

374 The Cosmic Microwave Background (CMB) is the primordial light from the early universe
375 when Hydrogen atoms formed from the free electron and proton soup in the early universe. The
376 CMB is the earliest light we can observe; released when the universe was about 380,000 years old.
377 Then we look at how the simulated universes look like compared to what we see. Figure 2.4 is the
378 most recent CMB image from the Plank satellite after subtracting the average value and masking the
379 galactic plane [10]. Redder regions indicate a slightly hotter region in the CMB, and blue indicates
380 colder. The intensity variations are on the order of 1 in 1000 with respect to the average value.

381 The Cosmic Microwave Background shows that the universe had DM in it from an incredibly
382 early stage. To measure the DM, Dark Energy, and matter fractions of the universe from the CMB,
383 the image is analyzed into a power spectrum, which shows the amplitude of the fluctuations as
384 a function of spherical multipole moments. Λ CDM provides the best fit to the power spectra of
385 the CMB as shown in Figure 2.5. The CMB power spectrum is quite sensitive to the fraction
386 of each energy contribution in the early universe. Low l modes are dominated by variations
387 in gravitational potential. Intermediate l emerge from oscillations in photon-baryon fluid from

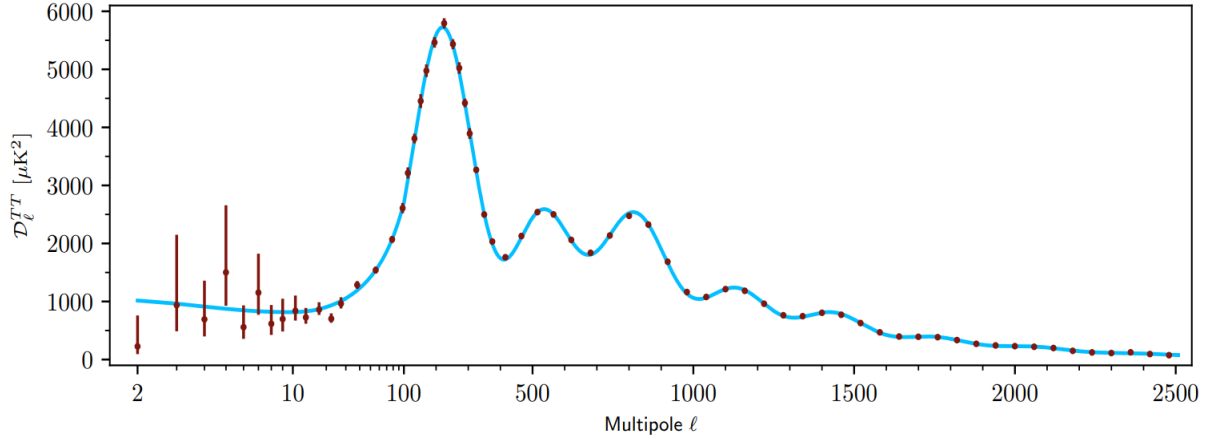


Figure 2.5 Observed Cosmic Microwave Background power spectrum as a function of multipole moment from Plank [10]. Blue line is best fit model from Λ CDM. Red points and lines are data and error, respectively.

388 competing baryon pressures and gravity. High l is a damped region from the diffusion of photons
 389 during electron-proton recombination. [1]

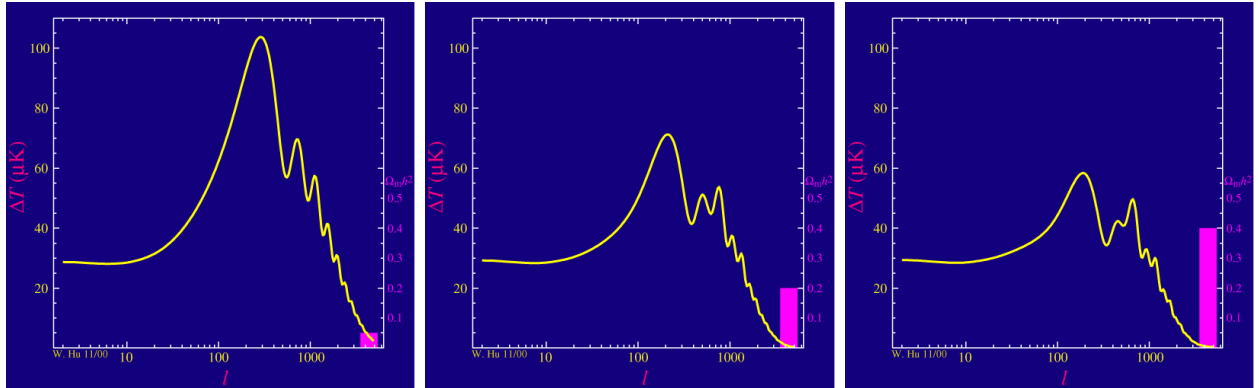


Figure 2.6 Predicted power spectra of CMB for different $\Omega_m h^2$ values for fixed baryon density from [11]. (left) Low $\Omega_m h^2$ increases the prominence of first and second peaks. (middle) $\Omega_m h^2$ is most similar to the observed power spectrum. The second and third peaks are similar in height. (right) $\Omega_m h^2$ is large which suppresses the first peak and raises the prominence of the third peak.

390 The harmonics would look quite different for a universe with less DM. Figure 2.6 demonstrates
 391 the effect $\Omega_m h^2$ has on the expected power spectrum for fixed baryon matter density. [11] Sweeping
 392 $\Omega_m h^2$ in this way clearly shows the effect dark matter has on the CMB power spectrum. The
 393 observations fit well with the Λ CDM model, and the derived fractions are as follows. The matter
 394 fraction: $\Omega_m = 0.3153$; and the baryon fraction: $\Omega_b = 0.04936$ [10]. Plank's observations also
 395 provide a measure of the Hubble constant, H_0 . H_0 especially has seen a growing tension in the

396 past decade that continues to deepened with observations from instruments like the James Webb
397 Telescope [12, 13]. As Hubble tensions deepen, we may find that perhaps Λ **CDM**, despite its
398 successes, is missing some critical physics.

399 Overall, the Newtonian motion of stars in galaxies, weak lensing from galactic clusters, and
400 power spectra from primordial light form a compelling body of research in favor of dark matter.
401 It takes another leap of theory and experimentation to make observations of DM that are non-
402 gravitational in nature. In Section 2.3, the evidence for DM implies strongly that the DM is matter
403 and not a lost parameter in the gravitational fields between massive objects. Finally, if we take one
404 axiom: that this matter has quantum behavior, such as being described by some Bohr wavelength
405 and abiding by some fermion or boson statistics; then we arrive at particle dark matter. One particle
406 DM hypothesis is the Weakly Interacting Massive Particle (WIMP). This DM candidate theory is
407 discussed further in the next section and is the focus of this thesis.

408 **2.4 Searching for Dark Matter: Particle DM**

409 Section 2.4 shows the Standard Model of particle physics and is currently the most accurate
410 model for the dynamics of fundamental particles like electrons and photons. The current status
411 of the SM does not have a viable DM candidate. When looking at the standard model, we can
412 immediately exclude any charged particle because charged particles interact strongly with light.
413 Specifically, this will rule out the following charged, fundamental particles: $e, \mu, \tau, W, u, d, s, c, t, b$
414 and their corresponding antiparticles. Recalling from Section 2.2 that DM must be long-lived and
415 stable over the age of the universe which excludes all SM particles with decay half-lives at or shorter
416 than the age of the universe. The lifetime constraint additionally eliminates the Z and H bosons.
417 Finally, the candidate DM needs to be somewhat massive. Recall from Section 2.2 that DM is cold
418 or not relativistic through the universe. This eliminates the remaining SM particles: $\nu_{e,\mu,\tau}, g, \gamma$ as
419 DM candidates. Because there are no DM candidates within the SM, the DM problem strongly
420 hints to physics beyond the SM (BSM).

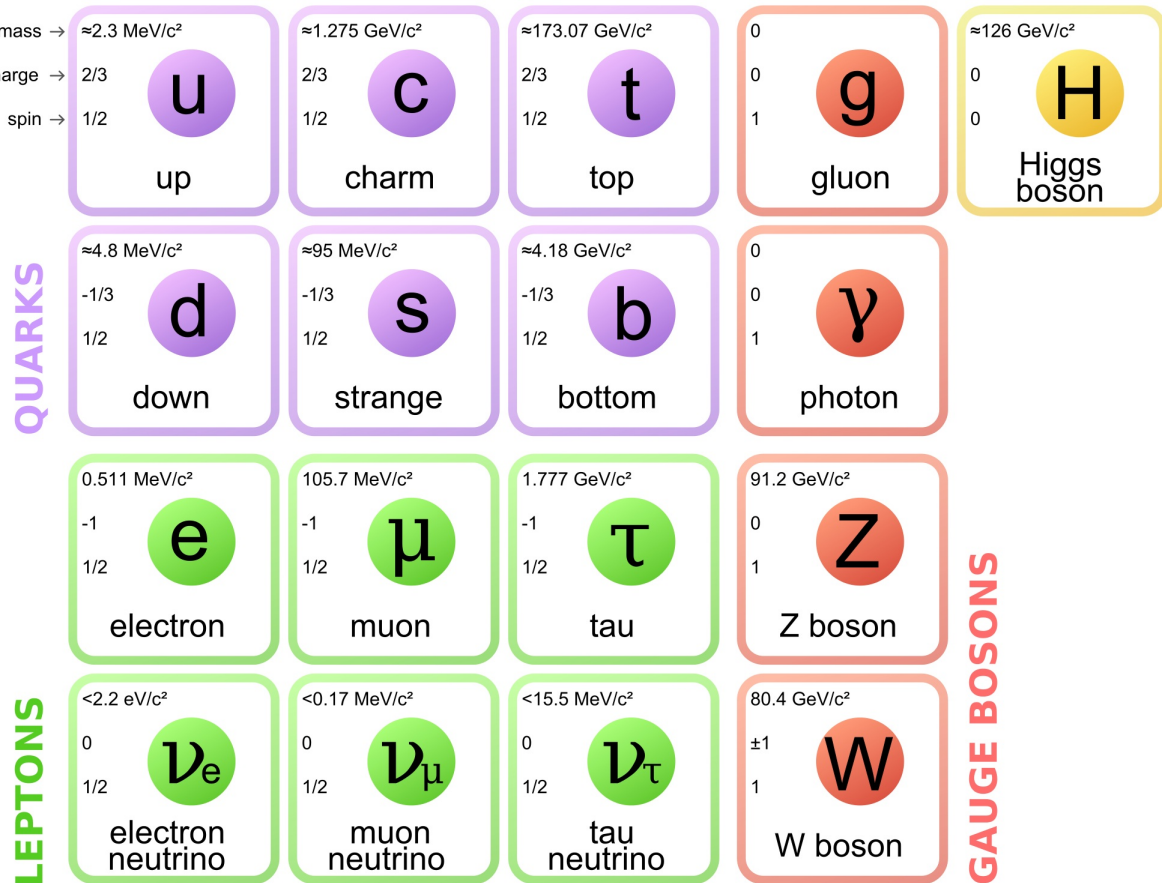


Figure 2.7 The Standard Model (SM) of particle physics. Figure taken from <http://www.quantumdiaries.org/2014/03/14/the-standard-model-a-beautiful-but-flawed-theory/>

421 2.4.1 Shake it, Break it, Make it

422 When considering DM that couples in some way with the SM, the interactions are roughly
 423 demonstrated by interaction demonstrated in Figure 2.8. The figure is a simplified Feynman
 424 diagram where the arrow of time represents the interaction modes of: **Shake it, Break it, Make it.**

425 **Shake it** refers to the direct detection of dark matter. Direct detection interactions start with
 426 a free DM particle and an SM particle. The DM and SM interact via elastic or inelastic collision
 427 and recoil away from each other. The DM remains in the dark sector and imparts some momentum
 428 onto the SM particle. The hope is that the momentum imparted onto the SM particle is sufficiently
 429 high enough to pick up with extremely sensitive instruments. Because we cannot create the DM in
 430 the lab, a direct detection experiment must wait until DM is incident on the detector. Most direct
 431 detection experiments are therefore placed in low-background environments with inert detection

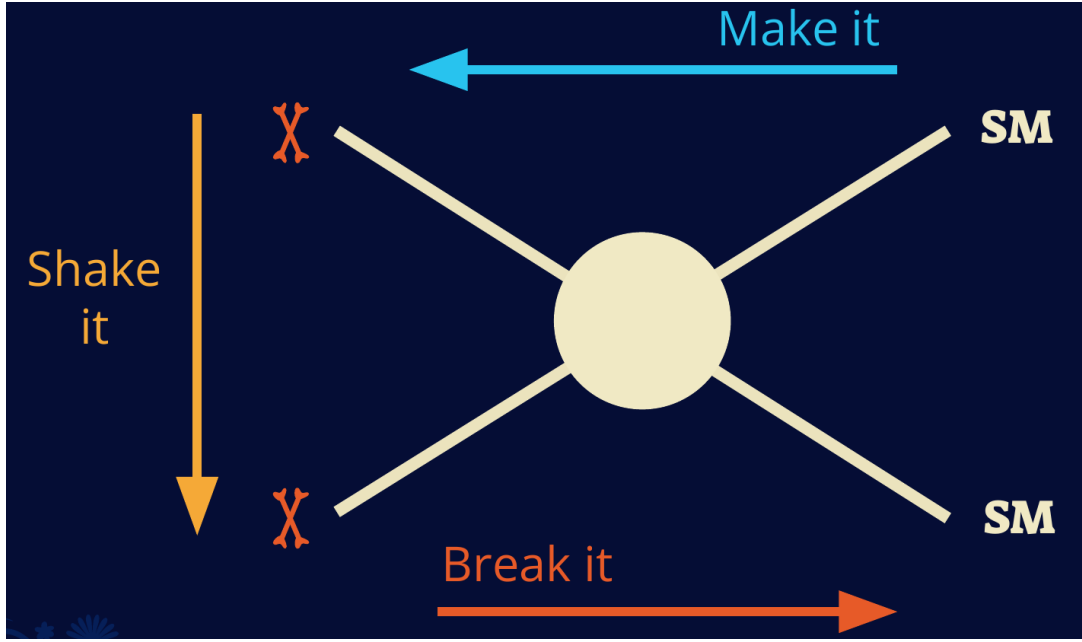


Figure 2.8 Simplified Feynman diagram demonstrating different ways DM can interact with SM particles. The 'X's refer to the DM particles whereas the SM refer to fundamental particles in the SM. The large circle in the center indicates the vertex of interaction and is purposely left vague. The colored arrows refer to different directions of time as well as their respective labels. The arrows indicate the initial and final state of the DM -SM interaction in time.

432 media like the noble gas Xenon. [14]

433 **Make it** refers to the production of DM from SM initial states. The experiment starts with
 434 particles in the SM. These SM particles are accelerated to incredibly high energies and then collide
 435 with each other. In the confluence of energy, DM hopefully emerges as a byproduct of the SM
 436 annihilation. Often it is the collider experiments that are energetic enough to hypothetically produce
 437 DM. These experiments include the world-wide collaborations ATLAS and CMS at CERN where
 438 proton collide together at extreme energies. The DM searches, however, are complex. DM likely
 439 does not interact with the detectors and lives long enough to escape the detection apparatus of
 440 CERN's colliders. This means any DM production experiment searches for an excess of events
 441 with missing momentum or energy in the events. An example event with missing transverse
 442 momentum is shown in Figure 2.9. The missing momentum with no particle tracks implies a
 443 neutral particle carried the energy out of the detector. However, there are other neutral particles
 444 in the SM, like neutrons or neutrinos, so any analysis has to account for SM signatures of missing

445 momentum. [15]

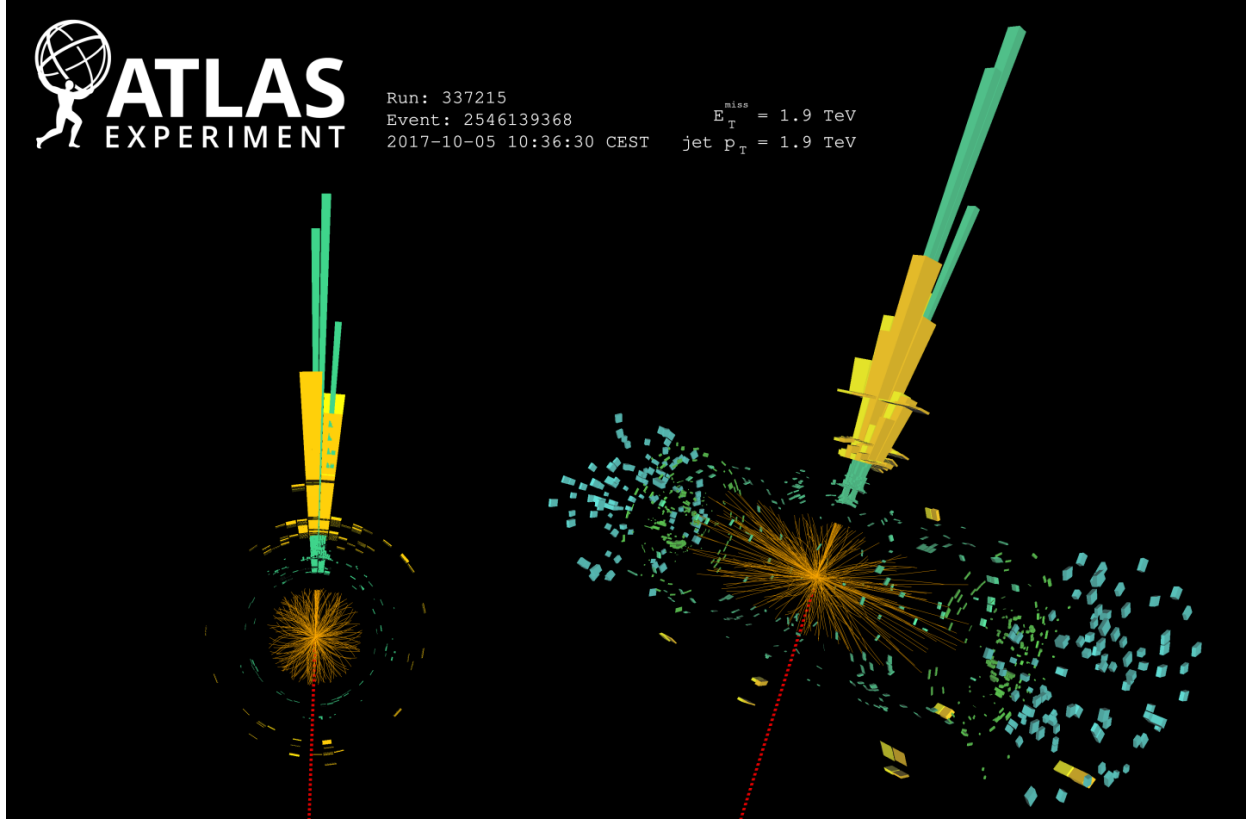


Figure 2.9 A single jet event in ATLAS detector from 2017 [16]. Jet momentum was observed to be 1.9 TeV. Missing transverse momentum was observed to be 1.9 TeV compared to the initial transverse momentum of the event was 0. Implied MET is traced by a red dashed line in event display.

446 2.4.2 Break it: Standard Model Signatures of Dark Matter through Indirect Searches

447 **Break it** refers to the creation of SM particles from the dark sector, and it is the primary focus
448 of this thesis. The interaction begins with DM or in the dark sector. The hypothesis is that this
449 DM will either annihilate with itself or decay and produce an SM byproduct. This method is
450 often referred to as the Indirect Detection of DM because we have no lab to directly control or
451 manipulate the DM. Therefore, most indirect DM searches are performed using observations of
452 known DM densities among the astrophysical sources. The strength is that we have the whole of the
453 universe and its 13.6-billion-year lifespan to use as a detector and particle accelerator. Additionally,
454 locations of dark matter are well cataloged since it was astrophysical observations that presented

455 the problem of DM in the first place.

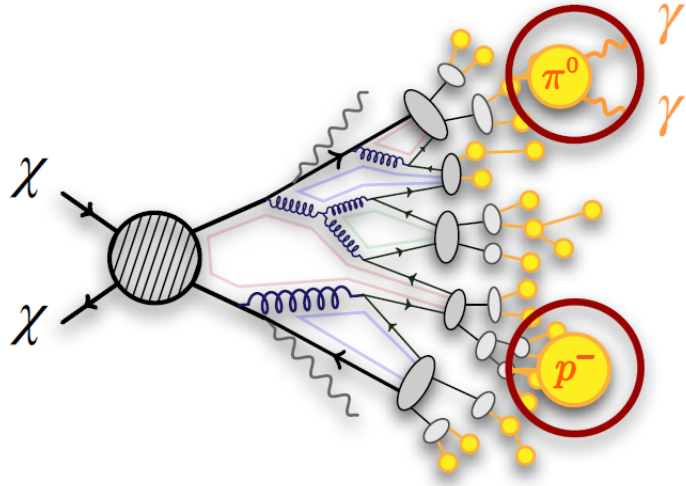


Figure 2.10 More detailed pseudo-Feynman diagram of particle cascade from dark matter annihilation into 2 quarks. The quarks hadronize and down to stable particles like γ or the anti-proton (p^-). Diagram pulled from ICRC 2021 presentation on DM annihilation search [17].

456 However, anything can happen in the universe. There are many difficult to deconvolve back-
457 grounds when searching for DM. One prominent example is the galactic center. We know the
458 galactic center has a large DM content because of stellar kinematics in our Milky Way and DM halo
459 simulations. Yet, any signal from the galactic center is challenging to parse apart from the extreme
460 environment of our supermassive black hole, unresolved sources, and diffuse emission from the
461 interstellar medium [18]. Despite the challenges, any DM model that yields evidence in the other
462 two observation methods, **Shake it or Make it** must be corroborated with indirect observations of
463 the known DM sources. Without corroborating evidence, DM observation in the lab is hard-pressed
464 to demonstrate that it is the model contributing to the DM seen at the universal scale.

465 In the case of WIMP DM, signals are described in terms of primary SM particles produced
466 from DM decay or annihilation. The SM initial state particles are then simulated down to stable
467 final states such as the γ , ν , p , or e which can traverse galactic lengths to reach Earth.

468 Figure 2.10 shows the quagmire of SM particles that emerges from SM initial states that are not
469 stable [17]. There are many SM particles with varying energies that can be produced in such an

470 interaction. For any arbitrary DM source and stable SM particle, the SM flux from DM annihilating
 471 to a neutral particle in the SM, ϕ , from a region in the sky is described by the following.

$$\frac{d\Phi_\phi}{dE_\phi} = \frac{\langle\sigma v\rangle}{8\pi m_\chi^2} \frac{dN_\phi}{dE_\phi} \times \int_{\text{source}} d\Omega \int_{l.o.s} \rho_\chi^2 dl(r, \theta') \quad (2.4)$$

472 In Equation (7.1), $\langle\sigma v\rangle$ is the velocity-weighted annihilation cross-section of DM to the SM. m_χ
 473 refers to the mass of DM, noted with Greek letter χ . $\frac{dN_\phi}{dE_\phi}$ is the N particle flux weighted by the
 474 particle energy. An example is provided in Figure 2.11 for the γ final state. The integrated terms
 475 are performed over the solid angle, $d\Omega$, and line of sight, l.o.s. ρ is the density of DM for a
 476 location (r, θ') in the sky. The terms left of the '×' are often referred to as the particle physics
 477 component. The terms on the right are referred to as the astrophysical component. For decaying
 478 DM, the equation changes to...

$$\frac{d\Phi_\phi}{dE_\phi} = \frac{1}{4\pi\tau m_\chi} \frac{dN_\phi}{dE_\phi} \times \int_{\text{source}} d\Omega \int_{l.o.s} \rho_\chi dl(r, \theta') \quad (2.5)$$

479 In Equation (2.5), τ is the decay lifetime of the DM. Just as in Equation (7.1), the left and
 480 right terms are the particle physics and the astrophysical components respectively. The integrated
 481 astrophysical component of Equation (7.1) is often called the J-Factor. Whereas the integrated
 482 astrophysical component of Equation (2.5) is often called the D-Factor.

483 Exact DM $\text{DM} \rightarrow \text{SM SM}$ branching ratios are not known, so it is usually assumed to go 100%
 484 into an SM particle/anti-particle. Additionally, when a DM annihilation or decay produces one of
 485 the neutral, long-lived SM particles (ν or γ), the particle is traced back to a DM source. For DM
 486 above GeV energies, there are very few SM processes that can produce particles with such a high
 487 energy. Seeing such a signal would almost certainly be an indication of the presence of dark matter.
 488 Fortunately, the universe provides us with the largest volume and lifetime ever for a particle physics
 489 experiment.

490 2.5 Sources for Indirect Dark Matter Searches

491 The first detection of DM relied on optical observations. Since then, we have developed new
 492 techniques to find DM dense regions. As described in Section 2.3.1, many DM dense regions were
 493 through observing galactic rotation curves. Our Milky Way galaxy is among DM dense regions

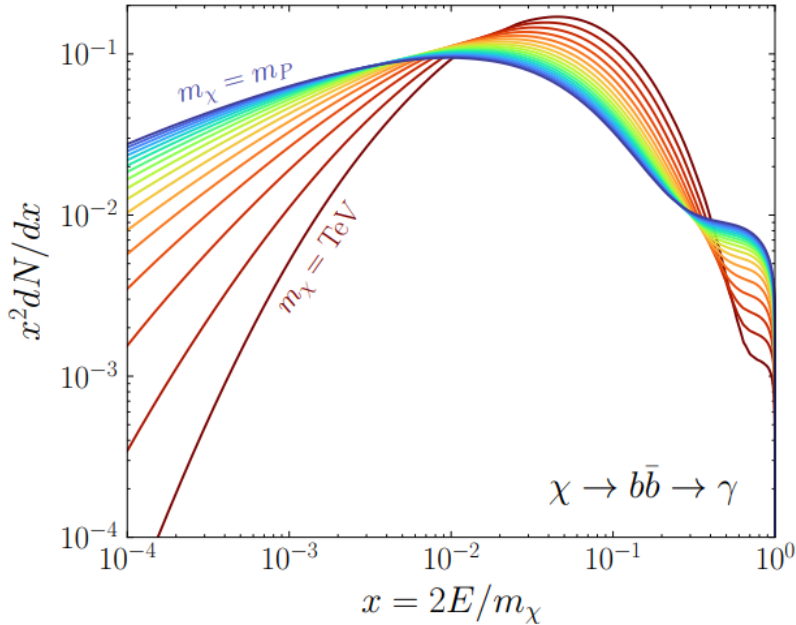


Figure 2.11 Dark Matter (DM) decay spectrum for $b\bar{b}$ initial state and γ final state. Redder spectra are for larger DM masses. Bluer spectra are light DM masses. x is a unitless factor defined as the ratio of the mass of DM, m_χ , and the final state particle energy E_γ . Figure from [19].

discovered, and it is the largest nearby DM dense region to look at. Additionally, the DM halo surrounding the Milky Way is clumpy [18]. There are regions in the DM halo of the Milky Way that have more DM than others that have captured gas over time. These sub-halos were dense enough collapse gas and form stars. These apparent sub galaxies are known as dwarf spheroidal galaxies and are the main sources studied in this thesis. Each source type comes with different trade-offs. Galactic Center studies will be very sensitive to the assumed distribution of DM. The central DM density can vary substantially as demonstrated in Figure 2.12. At distances close to the center of the galaxy, or small r , the differences in DM densities can be 3-4 orders of magnitude. Searches toward the galactic center will therefore be quite sensitive to the assumed DM distribution.

Searches toward Dwarf Spheroidal Galaxies (dSph's) suffer from uncertainties in the DM density less than the galactic center studies. This is mostly from their diminutive size being smaller than the angular resolution of most γ -ray observatories [18]. The DM content dSph's are typically determined with the Virial theorem, Equation (2.1), and are usually majority DM [18] in mass. DSph's tend to be ideal sources to look at for DM searches. Their environments are quiet with little

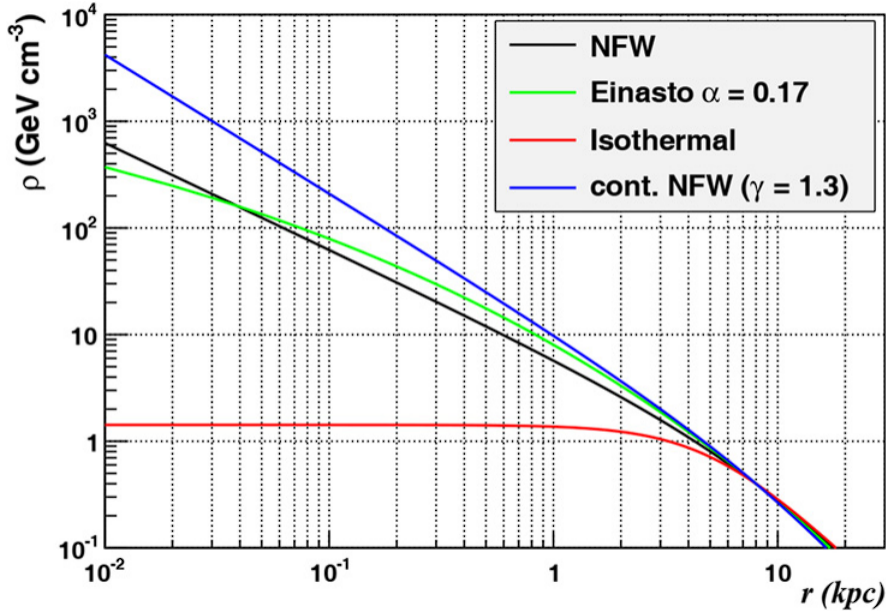


Figure 2.12 Different dark matter density profiles compared. Some models produce exceptionally large densities at small r [20].

508 astrophysical background. Unlike the galactic center, the most active components of dSph's are the
 509 stars within them versus a violent accretion disc around a black hole. All this together means that
 510 dSph's are among the best sources to look at for indirect DM searches. dSph's are the targets of
 511 focus for this thesis.

512 2.6 Multi-Messenger Dark Matter

513 Astrophysics entered a new phase in the past few decades that leverages our increasing sensitivity
 514 to SM channels and general relativity (GR). Up until the 21st century, astrophysical observations
 515 were performed with photons (γ) only. Astrophysics with this 'messenger' is fairly mature now.
 516 Novel observations of the universe have since only adjusted the sensitivity of the wavelength of
 517 light that is observed except at MeV energies. Gems like the CMB [10], and more have ultimately
 518 been observations of different wavelengths of light. Multi-messenger astrophysics proposes using
 519 other SM particles such the p^{+-} , or ν or gravitation waves predicted by general relativity.

520 The experiment LIGO had a revolutionary discovery in 2016 with the first detection of a binary
 521 black hole merger [21]. This opened the collective imagination to observing the universe through
 522 gravitational waves. There has also been a surge of interest in the neutrino (ν) sector. IceCube

523 demonstrated that we are sensitive to neutrinos in regions that correlate with significant photon
 524 emission like the galactic plane [22]. Neutrinos, like gravitational waves and light, travel mostly
 525 unimpeded from their source to our observatories. This makes pointing to the originating source
 526 of these messengers much easier than it is for cosmic rays which are deflected from their source by
 527 magnetic fields.

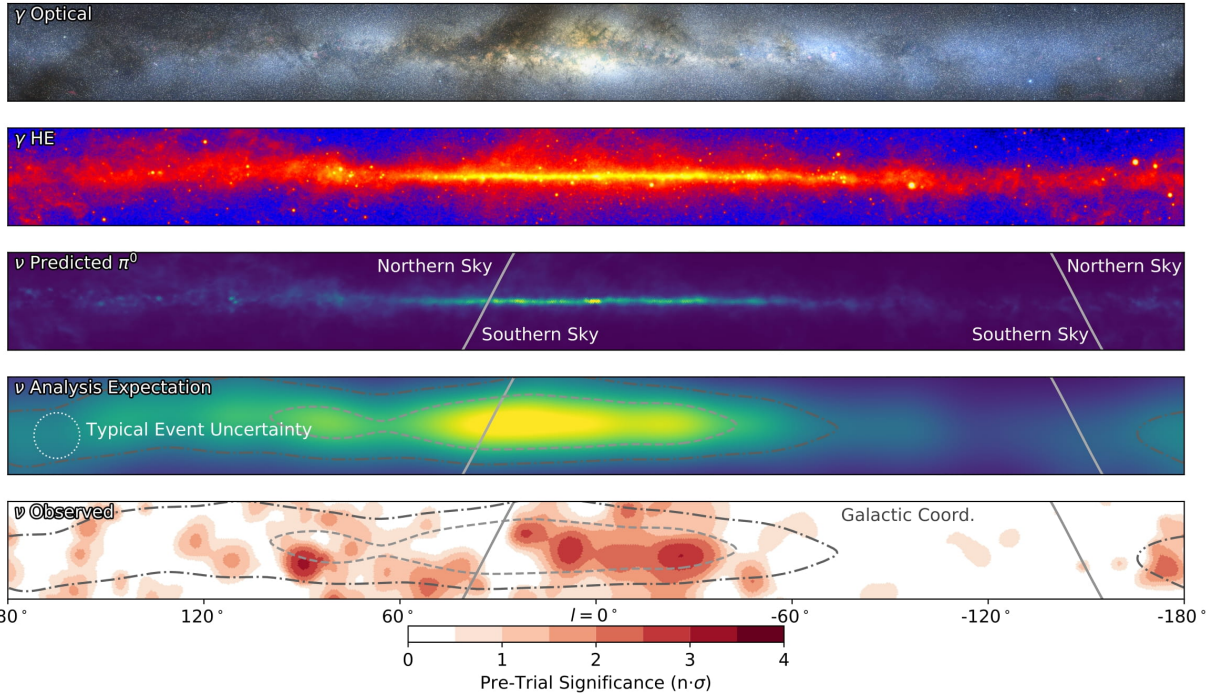


Figure 2.13 The Milky Way Galaxy in photons (γ) and neutrinos (ν) [22]. The Galactic center is at $l=0^\circ$ and is the brightest region in all panels. (top) An Optical color image of the Milky Way galaxy seen from Earth. Clouds of gas and dust obscure some light from stars. (2nd down) Integrated flux of γ -rays observed by the Fermi-LAT telescope [23]. (middle) Expected neutrino emission that corresponds with Fermi-LAT observations. (2nd up) Expected neutrino emission profile after considering detector systematics of IceCube. (bottom) Observed neutrino emission from region of the galactic plane. Substantial neutrino emission was detected.

528 The IceCube collaboration recently published a groundbreaking result of the Milky Way in
 529 neutrinos. The recent result from IceCube, shown in Figure 2.13, proves that we can make
 530 observations under different messenger regimes. The top two panels show the appearance of the
 531 galactic plane to different wavelengths of light. Some sources are more apparent in some panels,
 532 while others are not. This new channel is powerful because neutrinos are readily able to penetrate
 533 through gas and dust in the Milky Way. This new image also refines our understanding of how high

534 energy particles are produced. For example, the fit to IceCube data prefers neutrino production
 535 from the decay of π^0 [22].

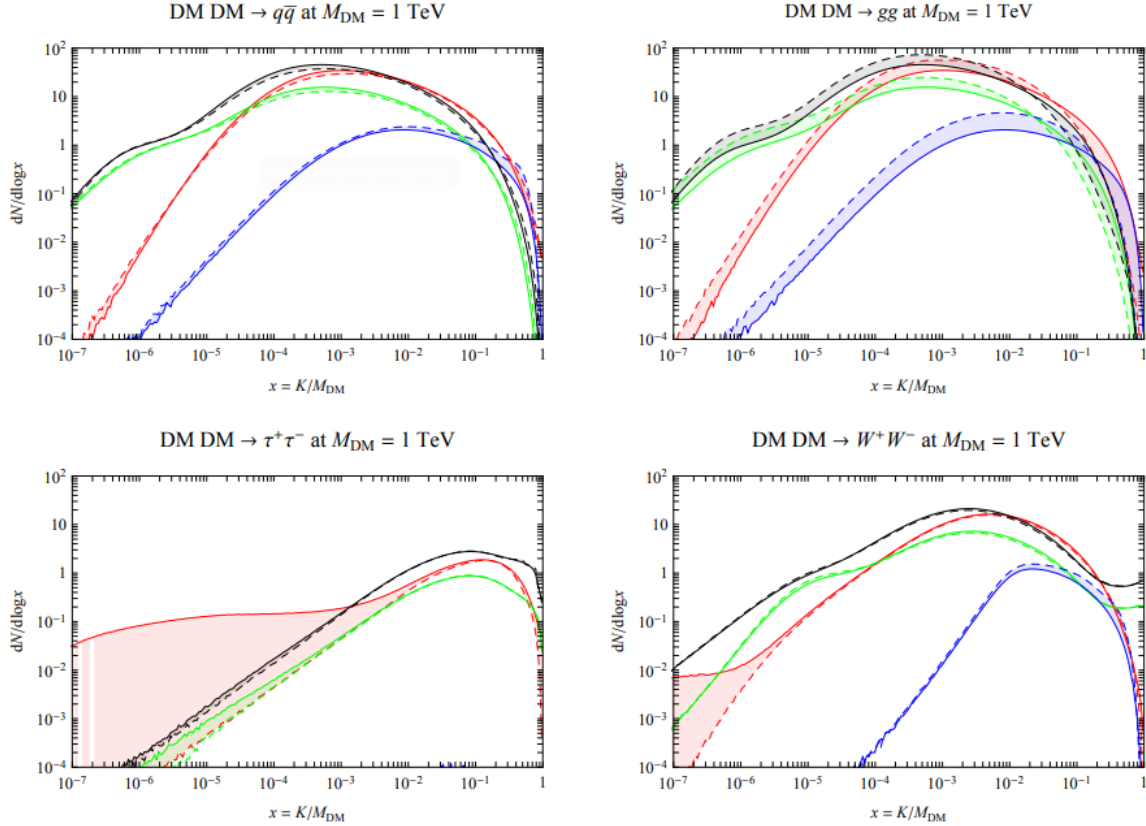


Figure 2.14 Dark Matter annihilation spectra for different final state particle and standard model annihilation channels [24]. Photons (red), e^\pm (green), \bar{p} (blue), ν (black).

536 Exposing our observations to more cosmic messengers greatly increases our sensitivity to
 537 rare processes. In the case of DM, Figure 2.14, there are many SM particles produced in DM
 538 annihilation. Among the final state fluxes are gammas and neutrinos. Charged particles are also
 539 produced however they would not likely make it to Earth since they will be deflected by magnetic
 540 fields between the source and Earth. This means observatories that can see the neutral messengers
 541 are especially good for DM searches and for combining data for a multi-messenger DM search.

CHAPTER 3

542 MULTIMESSENGER ASTROPHYSICS: DETECTING HIGH ENERGY NEUTRAL 543 MESSENGERS

544 3.1 Introduction

545 Before the 20th century, all astrophysics observations were optical in nature. We literally only
546 saw things with highly magnified optical observations. Then we discovered cosmic rays. cosmic
547 rays are charged particles, typically naked protons or H+. This was seen by Victor Hess in 19??.
548 Around the same time we discovered neutrinos from beta decay. Sometime around 1950 we started
549 to build neutrino detectors which were mostly sensitive to neutrinos from the sun. Finally, it was
550 theorized that compact objects like black holes and neutron stars would create waves in space-time
551 when they experience mergers or collisions.

552 In the 21st century, we have developed new observation techniques and detectors that are no only
553 sensitive to these four messengers - photons ([TODO: photon](#)), neutrinos ([TODO: nu](#)), Cosmic
554 Rays (CR), and Gravitational Wave (WV) - we're collect high energy versions of these events.
555 For the standad model particles, we're now sensitive to all messengers above the MeV eneryg
556 range. Additionally, the GW's were sensitive to are in the stellar mass black hole region and above
557 within our galactic neighborhood. This means were becoming sensitive to the fundamental physics
558 occuring within the universe and we can rely on the universe as a TeV+ particle accelerator. We
559 also have the abaility to correlate high energy events across messengers and gain new insights on
560 the processes that occur in our universe.

561 This thesis focuses on very high energy (VHE) gamma rays and neutrinos. These can both be
562 observed through the water cherenkov detection technique altho not exclusively. Methods on how
563 to detect and observe these neutral messengers are discussed Section 3.3 and Section 3.4

564 3.2 Charged Particles in a Medium

565 For high enery gamma-rays and neutrinos, we can exploit the same effect that charged particles
566 have with water. This effect is known as Cherenkov radiation. Cherenkov Radiation occurs when a
567 charged particle, usually electrons (e) or muons (μ), traverse a medium, like water, faster than the

568 speed of light in that medium. This is similar to sonic boom where an object moves through air
569 faster than the speed of sound in air. Cherenkov radiation can therefore be thought of as an 'optic
570 boom'. Many astro-particle physics experiments will use water as the medium as because water
571 has a unique set of properties ideal for charged particle tracking.



Figure 3.1 TODO: Show a nuclear reactor with cherenkov radiation[NEEDS A SOURCE][FACT CHECK THIS]

572 The frequency of light emitted due to cherenkov radiation follows the equation:

$$INSERT\ Cherenkov\ wavelength\ calc\ HERE. \quad (3.1)$$

573 The absorption spectra is shown in the following figure:

574 **3.3 Photons (γ)**

575 **3.4 Neutrinos (ν)**

576 **3.5 Opportunities to Combine for Dark Matter**



Figure 3.2 TODO: absorption spectrum of liquid and solid water[NEEDS A SOURCE][FACT CHECK THIS]

577

CHAPTER 4

HIGH ALTITUDE WATER CHERENKOV (HAWC) OBSERVATORY

578 **4.1 The Detector**

579 **4.2 Events Reconstruction and Data Acquisition**

580 **4.2.1 G/H Discrimination**

581 **4.2.2 Angle**

582 **4.2.3 Energy**

583 **4.3 Remote Monitoring**

584 **4.3.1 ATHENA Database**

585 **4.3.2 HOMER**

586

CHAPTER 5

ICECUBE NEUTRINO OBSERVATORY

587 **5.1 The Detector**

588 **5.2 Events Reconstruction and Data Acquisition**

589 **5.2.1 Angle**

590 **5.2.2 Energy**

591 **5.3 Northern Test Site**

592 **5.3.1 PIgeon remote dark rate testing**

593 **5.3.2 Bulkhead Construction**

CHAPTER 6

COMPUTATIONAL TECHNIQUES IN PARTICLE ASTROPHYSICS

595 **6.1 Neural Networks for Gamma/Hadron Separation**

596 **6.2 Parallel Computing for Dark Matter Analyses**

CHAPTER 7

597 GLORY DUCK: MULTI-WAVELENGTH SEARCH FOR DARK MATTTER 598 ANNIHILATION TOWARDS DWARF SPHEROIDAL GALAXIES

599 7.1 Introduction

600 The field of astrophysics now has several instruments and observatories sensitive to high
601 energy gamma-rays. The energy sensitivity for the modern gamma-ray program spans many orders
602 of magnitude. Figure 7.1 demonstrates these similar sensitivities across energies for the five
603 experiments: Fermi-LAT, HAWC, HESS, MAGIC, and VERITAS.

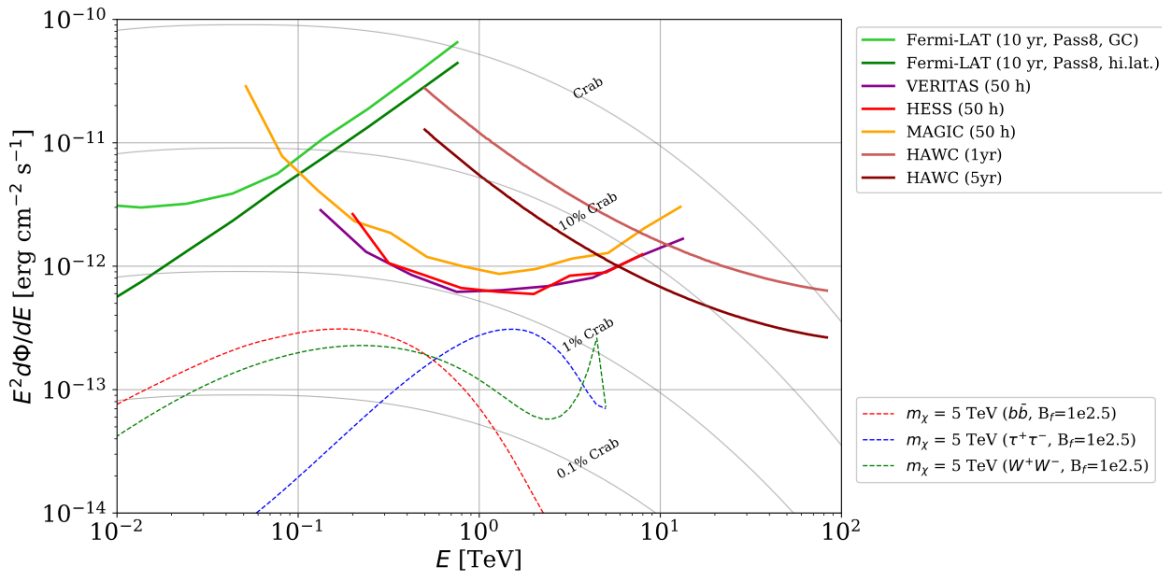


Figure 7.1 [NEEDS A SOURCE]Sensitivities of five gamma-ray experiments compared to percentages of the Crab nebula’s emission and dark matter annihilation. Solid lines present estimated sensitivities to power law spectra [FACT CHECK THIS]for each experiment. Green lines are Fermi-LAT sensitivities where lighter green is the sensitivity to the galactic center and light green is its sensitivity to higher declinations. Orange, red, and purple solid lines represent the MAGIC, HESS, and VERITAS 50 hour sensitivities respectively. The maroon and brown lines are the HAWC 1 year and 5 year sensitivities. Across four decades of gamma-ray energy, these experiments have similar sensitivities on the order 10^{-12} erg cm $^{-2}$ s $^{-1}$. The dotted lines are estimated dark matter fluxes assuming DM annihilating to bottom quarks (red), tau leptons (blue), and W bosons (green). Faded grey lines outline percentage flux of the Crab nebula.

604 Each of the five experiments featured in Figure 7.1 have independently searched for DM
605 annihilation from dwarf galaxies and set limits. Intriguingly, their similarities overlap in regions
606 where these observatories are less sensitive. This clearly motivates an analysis that combines data

607 from these five. Each experiment has unique gamma-ray detection methods and their weaknesses
608 and strengths can be leveraged with each other. The HAWC gamma-ray observatory is extensively
609 introduced in chapter 4, so it is not introduced here. A brief description of the remaining experiments
610 are in the following paragraphs.

611 The Large Area Telescope (LAT) is a pair conversion telescope mounted on the NASA Fermi
612 satellite in orbit 550 km above the Earth [25]. LAT's field of view covers about 20% of the
613 whole sky, and it sweeps the whole sky every 3 hours, approximately. LAT's gamma-ray energy
614 sensitivity ranges from 20 MeV up to 1 TeV. Previous DM searches towards dwarf galaxies using
615 Fermi-LAT are published in [26] and [27]

616 The High Energy Spectroscopic System (HESS), Major Atmospheric Gamma Imaging
617 Cherenkov (MAGIC), and Very Energetic Radiation Imaging Telescope Array System (VERI-
618 TAS) are arrays of Imaging Atmospheric Cherenkov Telescopes (IACT). These telescopes observe
619 the Cherenkov light emitted from gamma-ray showers in the Earth's atmosphere. The field for
620 these telescopes is no larger than 5° with energy sensitivities ranging from 30 GeV up to 100 TeV.
621 [28, 29, 30] IACTs are able to make precise observations in selected regions of the sky, however
622 can only be operated in ideal dark conditions. HESS's observations of the dwarves Sculptor and
623 Carina were between January 2008 and December 2009. HESS observations of Coma Berenices
624 were from 2010 to 2013, and Fornax was observed in 2010 [31, 32, 33]. MAGIC provided deep
625 observations of Segue1 between 2011 and 2013 [34]. MAGIC also provides data for three dwarves:
626 Coma Berenices, Draco, and Ursa Major II where observations were made in: January - June 2019
627 [35], March - September 2018 [35], and 2014 - 2016 [36] respectively. VERITAS provided data
628 for Boötes I, Draco, Segue 1, and Ursa Minor from 2009 to 2016 [37]

629 This chapter presents the Glory Duck analysis, the name given for the search for dark matter
630 annihilation from dwarf galaxies by combining data from the five gamma-ray observatories: Fermi-
631 LAT, HAWC, HESS, MAGIC, and VERITAS. Specifically, the methods in analysis and modeling
632 are presented for the HAWC gamma-ray observatory. This work was published to ??? and presented
633 at the International Cosmic Ray Conference in 2019, 2021, and 2023 [38, 39, 40] and more.

634 **7.2 Dataset and Background**

635 This section enumerates the data and background methods used for HAWC's study of the dwarf
636 spheroidal galaxies (dSph). Section 7.2.1 and Section 7.2.2 are most useful for fellow HAWC
637 collaborators looking to replicate the Glory Duck analysis.

638 **7.2.1 Itemized HAWC files**

- 639 • Detector Resolution: [response_aerie_svn_27754_systematics_best_mc_test_no](#)
640 [broadpulse_10pctlogchargesmearing_0.63qe_25kHzNoise_run5481_curvatu](#)
641 [re0_index3.root](#)
- 642 • Data Map: [maps-20180119/liff/maptree_1024.root](#)
- 643 • Spectral Dictionary: [DM_CirrelliSpectrum_dict_gammas.npy](#)
- 644 • Analysis wiki: https://private.hawc-observatory.org/wiki/index.php/Glory_Duck_Multi-Experiment_Dark_Matter_Search

646 **7.2.2 Software Tools and Development**

647 This analysis was performed using HAL and 3ML, in Python version 2[41, 42]. I built software
648 to implement the *Poor Particle Physicists' Cookbook* (PPPC) [43] DM spectral model and dSphs
649 spatial model from [44] for HAWC analysis. A NumPy version of this dictionary was made for
650 both Py2 and Py3. The code base for creating this dictionary is linked on my GitLab sandbox:

- 651 • Py2: [Dictionary Generator \(Deprecated\)](#)
- 652 • Py3: [PPPC2Dict](#)

653 The analysis was performed using the f_{hit} framework performed in the Crab paper[41]. The
654 Python2 NumPy dictionary file for gamma-ray final states is [dmCirSpecDict.npy](#). The corre-
655 sponding Python3 file is [DM_CirrelliSpectrum_dict_gammas.npy](#). These files can also be
656 used for decay channels and the PPPC describes how. [43]. All other software used for data

657 analysis, DM profile generation, and job submission to SLURM are also kept in my sandbox for
658 [the Glory Duck](#) project.

659 **7.2.3 Data Set and Background Description**

660 The HAWC data maps used for this analysis contain 1017 days of data between runs 2104
661 (2014-11-26) and 7476 (2017-12-20). They were generated from pass 4.0 reconstruction. The
662 analysis is performed using the f_{hit} energy binning scheme with bins (1-9) similar to what was done
663 for the Crab and previous HAWC dSph analysis. [41, 45]. Bin 0 was excluded as it has substantial
664 hadronic contamination and poor angular resolution.

665 This analysis was done on dwarf spheroidal (dSph) galaxies because of their large dark matter
666 (DM) content relative to baryonic. We consider the following to estimate the background to this
667 study.

- 668 • The dSphs are small in HAWC’s field of view, so the analysis is not sensitive to large or small
669 scale anisotropies.
- 670 • The dSphs used in this analysis are off the galactic plane.
- 671 • The dSphs are baryonically faint relative to their expected dark matter content and are not
672 expected to contain gamma-ray sources.

673 Therefor we make no additional assumptions on the background from our sources and use
674 HAWC’s standard direct integration method for background estimation [41]. It is possible for
675 gamma rays from DM annihilation to scatter in transit to HAWC via Inverse Compton Scattering
676 (ICS). This was investigated and its impact on the flux is basically zero. Supporting information
677 on this is in Section 7.6.1

678 **7.3 Analysis**

679 The expected differential photon flux from DM-DM annihilation to standard model particles
680 over solid angle is described by the familiar equation.

$$\frac{d\Phi_\gamma}{dE_\gamma} = \frac{\langle\sigma v\rangle}{8\pi m_\chi^2} \frac{dN_\gamma}{dE_\gamma} \times \int_{\text{source}} d\Omega \int_{l.o.s} \rho_\chi^2 dl(r, \theta') \quad (7.1)$$

681 Where $\langle \sigma v \rangle$ is the velocity weighted annihilation cross-section. $\frac{dN}{dE}$ is the expected differential
 682 number of photons produced at each energy per annihilation. M_χ is the rest mass of the supposed
 683 DM particle. J is the astrophysical J-factor and is defined as

$$J = \int \int \rho_\chi^2(l, \Omega) dl d\Omega \quad (7.2)$$

684 ρ_χ is the DM density. How each component is generated and considered for HAWC's analysis
 685 is presented in the following sections.

686 **7.3.1 $\frac{dN_\gamma}{dE_\gamma}$ - Particle Physics Component**

687 For this value, we import the PPPC with Electro-Weak (EW) corrections [43]. The spectrum is
 688 implemented as a model script in astromodels for 3ML. The PPPC model selected for this analysis
 689 included EW corrections. The EW corrections were previously not considered for HAWC and are
 690 significant for DM annihilating to EW coupled SM particles such as all leptons, and the γ , Z , and W
 691 bosons. [45]. Figure 7.2 demonstrates the significance of EW corrections for W boson annihilation.
 692 Tables from the PPPC were reformatted into python Numpy dictionaries for collaboration-wide use.
 693 A class in atromodels was created to include the EW correction from the PPPC and is aptly named
 694 `PPPCSpectra` within `DM_models.py`.

695 **7.3.2 J - Astrophysical Component**

696 The J-factor profiles for each source are imported from Geringer-Sameth (\mathcal{GS}) [44]. These
 697 were provided from the authors as $J(\theta)$, where θ is the angular separation from the center of the
 698 source. HAWC requires maps in terms of $\frac{dJ}{d\Omega}$, so the conversion from the maps was done in the
 699 following way.

700 First, convert the angular distances to solid angles

$$\Omega = 2 \cdot \pi(1 - \cos(\theta)) \quad (7.3)$$

701 which reduces with a small angle approximation to $\pi\theta^2$. Next, the central difference for both the ΔJ
 702 and $\Delta\theta$ value were calculated for the discretized form of $J(\theta)$ with the central difference stencil:

$$\Delta\phi_i = \phi_{i+1} - \phi_{i-1} \quad (7.4)$$

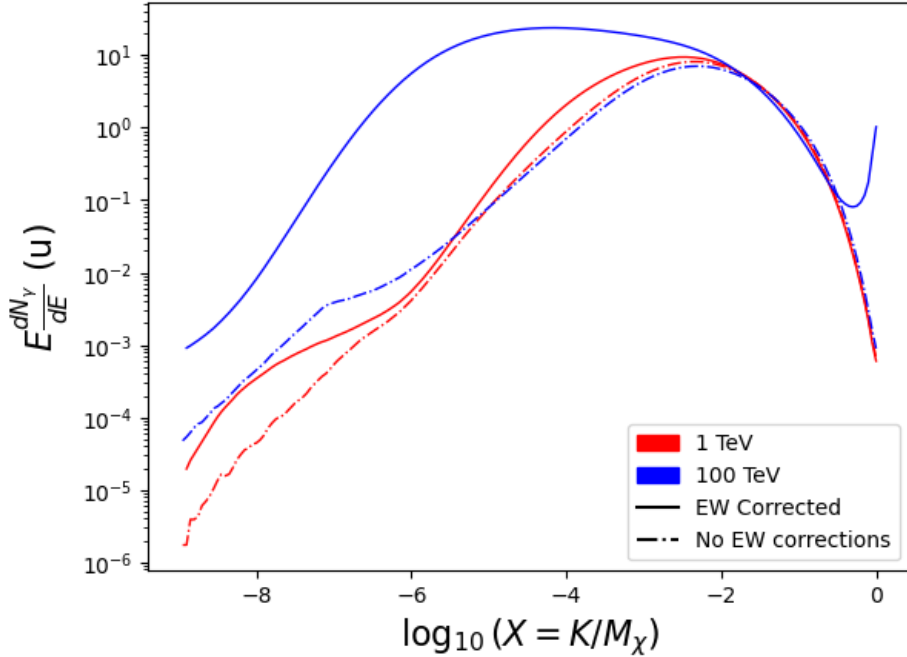


Figure 7.2 Effect of Electro-Weak (EW) corrections on expected DM annihilation spectrum for $\chi\chi \rightarrow W^-W^+$. Solid lines are spectral models that consider EW corrections. Dash-dot lines are spectral models without EW corrections. Red lines are models for $M_\chi = 1$ TeV. Blue lines represent models for $M_\chi = 100$ TeV. All models are sourced from the PPPC4DMID [43].

703 Where ϕ is either θ or J . These were done separately in case the grid spacing in θ was not uniform.
 704 Finally, these lists are divided so that we are left with approximation of the profile of $dJ/d\Omega$ that
 705 is a function of θ . Admittedly, this is an approximation method for the map which introduces
 706 small errors compared to the true profile estimate. This was checked as a systematic against the
 707 author's profiling of the spatial distribution and is documented in **TODO: Model dependant limit,**
 708 **remember the jfactors!**

709 With $\frac{dJ}{d\Omega}$, a map is generated, first by filling in the north-east quadrant of the map. This quadrant
 710 is then reflected twice, vertically then horizontally, to fill the full map. Maps are then normalized
 711 by dividing the discrete 2D integral of the map. The 2D integral was a simple height of bins,
 712 Newton's integral:

$$p^2 \cdot \sum_{i,j=0}^{N,M} \frac{dJ}{d\Omega}(\theta_{i,j}) \quad (7.5)$$

713 These maps are HEALpix maps with NSIDE 16384 and saved in the `.fits` format.

714 Another DM spatial distribution model from Bonnivard (\mathcal{B}) [46] was used for the complete

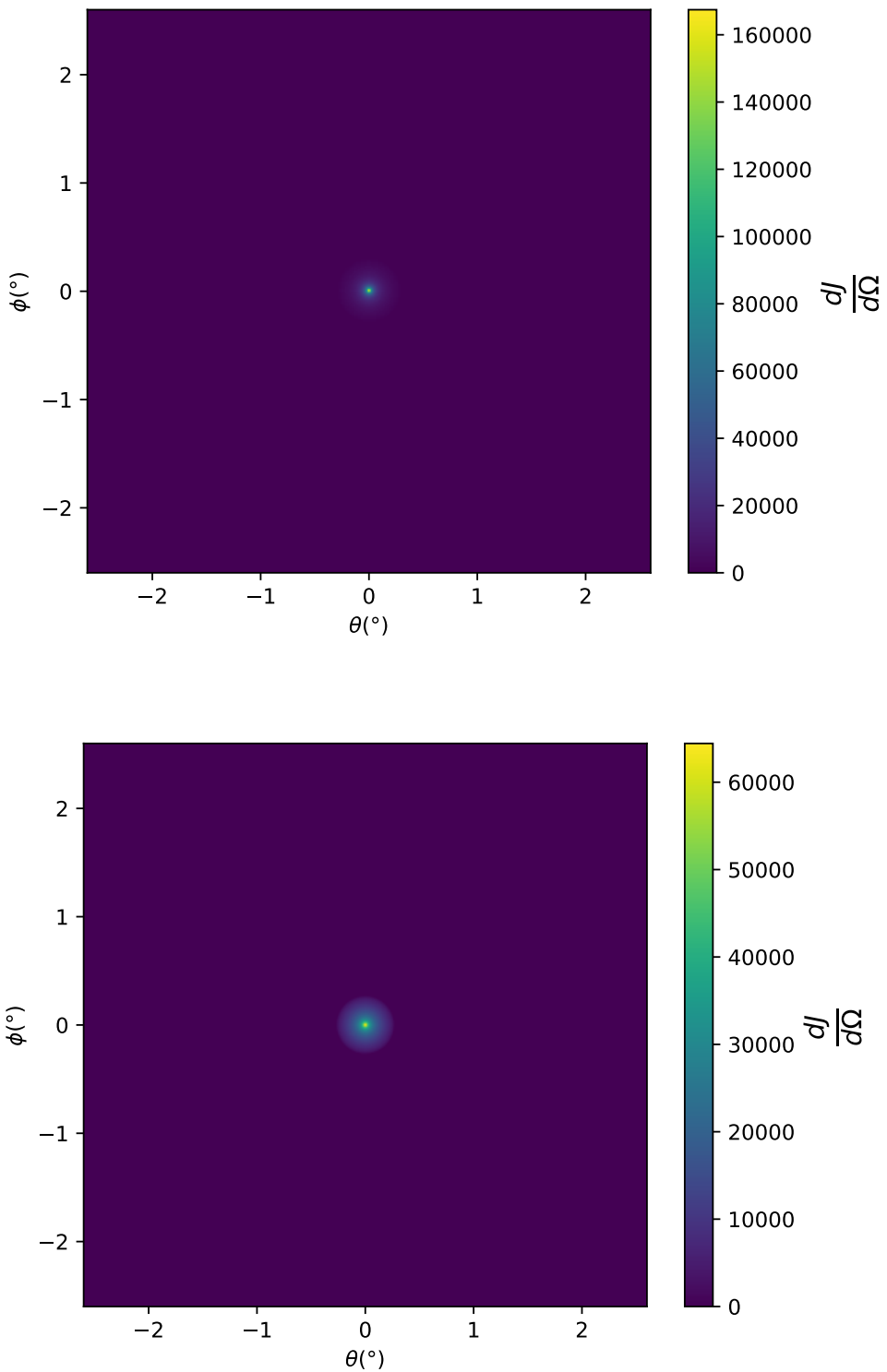


Figure 7.3 $\frac{dJ}{d\Omega}$ maps for Segue1 (top) and Coma Berenices (bottom). Origin is centered on the specific dwarf spheroidal galaxies (dSph). X and Y axes are the angular separation from the center of the dwarf. Plots of the remaining 11 dSph HAWC studied are linked in Section 7.2.2.

study. However, to save computational time, limits from \mathcal{GS} were scaled to \mathcal{B} instead of each experiment performing a full study a second time. How these models compare is demonstrated for each dSph in Figure 7.15 and Figure 7.16. Plots of these maps are provided for each source in the sandbox directory: `GD_mass_profiles`. Examples of the two most impactful dSphs, Segue1 and Coma Berenices are featured in Figure 7.3

7.3.3 Source Selection and Annihilation Channels

We use many of the dSph presented in our previous dSph DM search [45]. HAWC's sources for Glory Duck include Boötes I, Coma Berenices, Canes Venatici I + II, Draco, Hercules, Leo I, II, + IV, Segue 1, Sextans, and Ursa Major I + II. A full description of all sources used in Glory Duck is found in Table 7.1. Triangulum II was excluded from the Glory Duck analysis because of large uncertainties in its J-factor. Ursa Minor was excluded from HAWC's contribution to the combination because the source extension model extended Ursa Minor beyond HAWC's field of view. Ursa Minor was not expected to contribute significantly to the combined limit, so work was not invested in a solution to include Ursa Minor.

The DM annihilation channels probed for the Glory Duck combination include $b\bar{b}$, $e\bar{e}$, $\mu\bar{\mu}$, $\tau\bar{\tau}$, $t\bar{t}$, W^+W^- , and ZZ . A summary of all sources, with a description of each experiments' sensitivity to the source, is provided in Table 7.2.

7.3.4 Likelihood Methods

We perform a standard HAWC binned maximum likelihood analysis using f_{hit} bins 1-9. This analysis was performed using HAL and 3ML, in Python2 [41, 42]. With these tools we compute the max from the likelihood profiles and perform a ratio test to calculate the significance of each source. This analysis is identical to the previous dSph analysis [45] except the sources are treated as extended. For the vast majority of our sources, this extension is no greater than 2 degrees. We calculate the likelihood of each source and model, assuming events are Poisson distributed, with

$$\mathcal{L} = \prod_i \frac{(B_i + S_i)^{N_i} e^{-(B_i + S_i)}}{N_i!} \quad (7.6)$$

S_i is the sum of expected number of signal counts. B_i is the number of background counts

Table 7.1 Summary of the relevant properties of the dSphs used in the present work. Column 1 lists the dSphs. Columns 2 and 3 present their heliocentric distance and galactic coordinates, respectively. Columns 4 and 5 report the J -factors of each source given from the \mathcal{GS} and \mathcal{B} independent studies and their estimated $\pm 1\sigma$ uncertainties. The values $\log_{10} J$ (\mathcal{GS} set) [44] correspond to the mean J -factor values for a source extension truncated at the outermost observed star. The values $\log_{10} J$ (\mathcal{B} set) [46] are provided for a source extension at the tidal radius of each dSph. **Bolded sources are within HAWC's field of view and provided to the Glory Duck analysis.**

Name	Distance (kpc)	l, b ($^{\circ}$)	$\log_{10} J$ (\mathcal{GS} set) $\log_{10}(\text{GeV}^2\text{cm}^{-5}\text{sr})$	$\log_{10} J$ (\mathcal{B} set) $\log_{10}(\text{GeV}^2\text{cm}^{-5}\text{sr})$
Boötes I	66	358.08, 69.62	$18.24^{+0.40}_{-0.37}$	$18.85^{+1.10}_{-0.61}$
Canes Venatici I	218	74.31, 79.82	$17.44^{+0.37}_{-0.28}$	$17.63^{+0.50}_{-0.20}$
Canes Venatici II	160	113.58, 82.70	$17.65^{+0.45}_{-0.43}$	$18.67^{+1.54}_{-0.97}$
Carina	105	260.11, -22.22	$17.92^{+0.19}_{-0.11}$	$18.02^{+0.36}_{-0.15}$
Coma Berenices	44	241.89, 83.61	$19.02^{+0.37}_{-0.41}$	$20.13^{+1.56}_{-1.08}$
Draco	76	86.37, 34.72	$19.05^{+0.22}_{-0.21}$	$19.42^{+0.92}_{-0.47}$
Fornax	147	237.10, -65.65	$17.84^{+0.11}_{-0.06}$	$17.85^{+0.11}_{-0.08}$
Hercules	132	28.73, 36.87	$16.86^{+0.74}_{-0.68}$	$17.70^{+1.08}_{-0.73}$
Leo I	254	225.99, 49.11	$17.84^{+0.20}_{-0.16}$	$17.93^{+0.65}_{-0.25}$
Leo II	233	220.17, 67.23	$17.97^{+0.20}_{-0.18}$	$18.11^{+0.71}_{-0.25}$
Leo IV	154	265.44, 56.51	$16.32^{+1.06}_{-1.70}$	$16.36^{+1.44}_{-1.65}$
Leo V	178	261.86, 58.54	$16.37^{+0.94}_{-0.87}$	$16.30^{+1.33}_{-1.16}$
Leo T	417	214.85, 43.66	$17.11^{+0.44}_{-0.39}$	$17.67^{+1.01}_{-0.56}$
Sculptor	86	287.53, -83.16	$18.57^{+0.07}_{-0.05}$	$18.63^{+0.14}_{-0.08}$
Segue I	23	220.48, 50.43	$19.36^{+0.32}_{-0.35}$	$17.52^{+2.54}_{-2.65}$
Segue II	35	149.43, -38.14	$16.21^{+1.06}_{-0.98}$	$19.50^{+1.82}_{-1.48}$
Sextans	86	243.50, 42.27	$17.92^{+0.35}_{-0.29}$	$18.04^{+0.50}_{-0.28}$
Ursa Major I	97	159.43, 54.41	$17.87^{+0.56}_{-0.33}$	$18.84^{+0.97}_{-0.43}$
Ursa Major II	32	152.46, 37.44	$19.42^{+0.44}_{-0.42}$	$20.60^{+1.46}_{-0.95}$
Ursa Minor	76	104.97, 44.80	$18.95^{+0.26}_{-0.18}$	$19.08^{+0.21}_{-0.13}$

Table 7.2 Summary of dSph observations by each experiment used in this work. A ‘-’ indicates the experiment did not observe the dSph for this study. For Fermi-LAT, the exposure at 1 GeV is given. For HAWC, $|\Delta\theta|$ is the absolute difference between the source declination and HAWC latitude. HAWC is more sensitive to sources with smaller $|\Delta\theta|$. For IACTs, we show the zenith angle range, the total exposure, the energy range, the angular radius θ of the signal or ON region, the ratio of exposures between the background-control (OFF) and signal (ON) regions (τ), and the significance of gamma-ray excess in standard deviations, σ .

Source name	Fermi-LAT	HAWC	H.E.S.S, MAGIC, VERITAS						
	Exposure (10^{11} s m 2)	$ \Delta\theta $ ($^\circ$)	IACT	Zenith ($^\circ$)	Exposure (h)	Energy range (GeV)	θ ($^\circ$)	τ	S (σ)
Boötes I	2.6	4.5	VERITAS	15 – 30	14.0	100–41000	0.10	8.6	-1.0
Canes Venatici I	2.9	14.6	–	–	–	–	–	–	–
Canes Venatici II	2.9	15.3	–	–	–	–	–	–	–
Carina	3.1	–	H.E.S.S.	27 – 46	23.7	310 – 70000	0.10	18.0	-0.3
Coma Berenices	2.7	4.9	H.E.S.S.	47 – 49	11.4	550 – 70000	0.10	14.4	-0.4
Draco	3.8	38.1	MAGIC	5 – 37	49.5	60 – 10000	0.17	1.0	–
			MAGIC	29 – 45	52.1	70 – 10000	0.22	1.0	–
			VERITAS	25 – 40	49.8	120 – 70000	0.10	9.0	-1.0
Fornax	2.7	–	H.E.S.S.	11 – 25	6.8	230 – 70000	0.10	45.5	-1.5
Hercules	2.8	6.3	–	–	–	–	–	–	–
Leo I	2.5	6.7	–	–	–	–	–	–	–
Leo II	2.6	3.1	–	–	–	–	–	–	–
Leo IV	2.4	19.5	–	–	–	–	–	–	–
Leo V	2.4	–	–	–	–	–	–	–	–
Leo T	2.6	–	–	–	–	–	–	–	–
Sculptor	2.7	–	H.E.S.S.	10 – 46	11.8	200 – 70000	0.10	19.8	-2.2
Segue I	2.5	2.9	MAGIC	13 – 37	158.0	60 – 10000	0.12	1.0	-0.5
			VERITAS	15 – 35	92.0	80 – 50000	0.10	7.6	0.7
Segue II	2.7	–	–	–	–	–	–	–	–
Sextans	2.4	20.6	–	–	–	–	–	–	–
Ursa Major I	3.4	32.9	–	–	–	–	–	–	–
Ursa Major II	4.0	44.1	MAGIC	35 – 45	94.8	120 – 10000	0.30	1.0	-2.1
Ursa Minor	4.1	–	VERITAS	35 – 45	60.4	160 – 93000	0.10	8.4	-0.1

740 observed. N_i is the total number of counts. The i th bin is iterated over spatial and f_{hit} . Then we
 741 combine the profiles across all five experiments. The profile likelihood ratio λ as a function of
 742 annihilation cross-section $\langle\sigma v\rangle$ is computed by:

$$\lambda(\langle\sigma v\rangle | \mathcal{D}_{\text{dSphs}}) = \frac{\mathcal{L}(\langle\sigma v\rangle; \hat{\nu} | \mathcal{D}_{\text{dSphs}})}{\mathcal{L}(\widehat{\langle\sigma v\rangle}; \hat{\nu} | \mathcal{D}_{\text{dSphs}})} \quad (7.7)$$

744 for a considered annihilation channel and DM mass.

745 **TODO: Section pasted from paper. Rephrase cause plagiarism is a thing.** As mentioned pre-
 746 viously, each experiment computes the \mathcal{L}_{lk} from Equation (7.7) differently. The remainder of
 747 this section highlights the differences in this calculation across the experiments. Four experiments,
 748 namely *Fermi*-LAT, H.E.S.S., HAWC and MAGIC, use a binned likelihood to compute the \mathcal{L}_{lk} . For
 749 these experiments, for each observation \mathcal{D}_{lk} of a given dSph l carried out using a given gamma-ray
 750 detector k , the binned likelihood function is:

$$\mathcal{L}_{lk}(\langle\sigma v\rangle; J_l, \nu_{lk} | \mathcal{D}_{lk}) = \prod_{i=1}^{N_E} \prod_{j=1}^{N_P} \left[\mathcal{P}(s_{lk,ij}(\langle\sigma v\rangle, J_l, \nu_{lk}) + b_{lk,ij}(\nu_{lk}) | N_{lk,ij}) \right] \times \mathcal{L}_{lk,\nu}(\nu_{lk} | \mathcal{D}_{\nu_{lk}}) \quad (7.8)$$

751 where N_E and N_P are the number of considered bins in reconstructed energy and arrival
 752 direction, respectively; \mathcal{P} represents a Poisson PDF for the number of gamma-ray candidate events
 753 $N_{lk,ij}$ observed in the i -th bin in energy and j -th bin in arrival direction, when the expected number
 754 is the sum of the expected mean number of signal events s_{ij} (produced by DM annihilation) and of
 755 background events b_{ij} ; $\mathcal{L}_{lk,\nu}$ is the likelihood term for the extra ν_{lk} nuisance parameters that vary
 756 from one instrument k to another. The expected counts for signal events s_{ij} for a given dSph l and
 757 detector k is given by:

$$s_{ij}(\langle\sigma v\rangle, J) = \int_{E'_{\min,i}}^{E'_{\max,i}} dE' \int_{P'_{\min,j}}^{P'_{\max,j}} d\Omega' \int_0^\infty dE \int_{\Delta\Omega_{tot}} d\Omega \int_0^{T_{\text{obs}}} dt \frac{d^2\Phi(\langle\sigma v\rangle, J)}{dEd\Omega} \text{IRF}(E', P' | E, P, t) \quad (7.9)$$

758 where E' and E are the reconstructed and true energies, P' and P the reconstructed and true
 759 arrival directions; $E'_{\min,i}$, $P'_{\min,j}$, $E'_{\max,i}$, and $P'_{\max,j}$ are their lower and upper limits of the i -th
 760 energy bin and the j -th arrival direction bin; T_{obs} is the (dead-time corrected) total observation

761 time; t is the time along the observations; $d^2\Phi/dEd\Omega$ is the DM flux in the source region (see
 762 Equation (7.1)); and $\text{IRF}(E', P' | E, P, t)$ is the IRF, which can be factorized as the product of the
 763 effective collection area of the detector $A_{\text{eff}}(E, P, t)$, the PDFs for the energy estimator $f_E(E' | E, t)$,
 764 and arrival direction $f_P(P' | E, P, t)$ estimators. Note that for Fermi-LAT, HAWC, MAGIC, and
 765 VERITAS the effect of the finite angular resolution is taken into account through the convolution
 766 of $d\Phi/dEd\Omega$ with f_P in Equation (7.9), whereas in the cases of H.E.S.S. f_P is approximated by a
 767 delta function. This approximation has been made in order to maintain compatibility of the result
 768 with what has been previously published. The difference introduced by this approximation is $< 5\%$
 769 for all considered dSphs. **TODO: End of paper section**

770 From Equation (7.7), we can compute the test statistic (TS) with the ratio test:

$$\text{TS} = -2 \ln \left(\frac{\mathcal{L}}{\mathcal{L}^{\max}} \right). \quad (7.10)$$

771 \mathcal{L}^{\max} here is equivalent to $\mathcal{L}(N_i, B_i, S_i = 0)$ or no signal counts.

772 7.4 HAWC Results

773 13 of the 20 dSphs considered for the Glory Duck analysis are within HAWC's field of view.
 774 These dSph are analyzed for emission from DM annihilation according to the likelihood method
 775 described in Section 7.3.4. The 13 likelihood profiles are then combined to create a combined limit
 776 on the dark matter cross-section. This combination is done for the 7 annihilation channels used in
 777 the Glory Duck analysis. Figure 7.5 shows the combined limit for all annihilation channels with
 778 HAWC only observations. We also perform 300 studies of Poisson trials on the background. These
 779 trials are used to produce HAWC Brazil bands which were shared with the other collaborators for
 780 combined Brazil Bands. The results on fitting to HAWC's poisson trials of the DM hypothesis is
 781 shown in Figure 7.6 for seven of the DM annihilation channels.

782 No DM was found in HAWC observations. The limits are dominated by the dSph Segue1 and
 783 Coma Berenices. The remaining 11 dSphs do no contribute significantly to the limit. Even though
 784 some of the remaining dSphs have large J-factors, they are towards the edge of HAWC's field of
 785 view where this analysis is less sensitive.

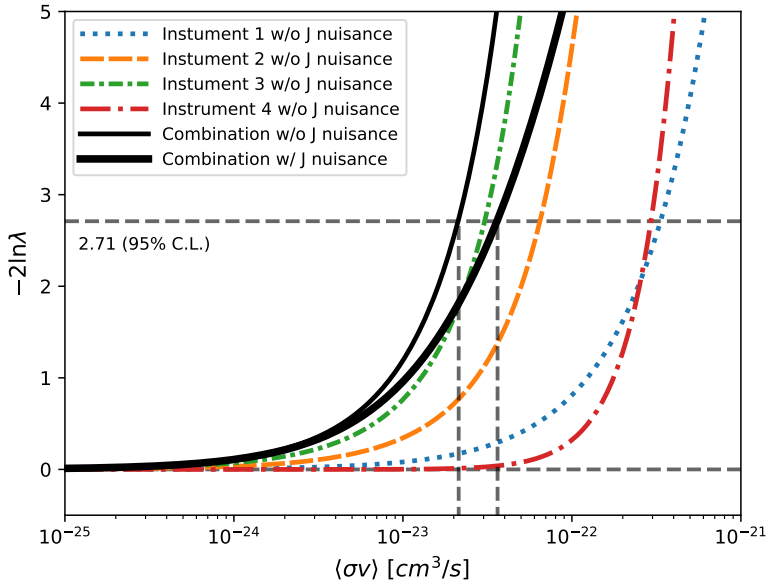


Figure 7.4 Illustration of the combination technique showing a comparison between $-2 \ln \lambda$ provided by four instruments (colored lines) from the observation of the same dSph without any J nuisance and their sum, *i.e.* the resulting combined likelihood (thin black line). According to the test statistics of Equation (7.10), the intersection of the likelihood profiles with the line $-2 \ln \lambda = 2.71$ indicates the 95% C.L. upper limit on $\langle\sigma v\rangle$. The combined likelihood (thin black line) shows a smaller value of upper limit on $\langle\sigma v\rangle$ than those derived by individual instruments. We also show the uncertainties on the J -factor affects the combined likelihood and degrade the upper limit on $\langle\sigma v\rangle$ (thick black line). All likelihood profiles are normalized so that the global minimum $\widehat{\langle\sigma v\rangle}$ is 0. We note that each profile depends on the observational conditions in which a target object was observed. The sensitivity of a given instrument can be degraded and the upper limits less constraining if the observations are performed in non optimal conditions such as a high zenith angle or a short exposure time.

786 7.5 Glory Duck Combined Results

787 The crux of this analysis is that HAWC's results are combined with 4 other gamma-ray obser-
 788 vatories: Fermi-LAT, H.E.S.S., MAGIC, and VERITAS. The complete joint likelihood for the l -th
 789 dSph is the product of likelihood functions of the 5 experiments.

790 **TODO:** place holder for results

791 The *partial* joint likelihood function for gamma-ray observations of each dSph ($\mathcal{L}_{dSph,l}$) is
 792 written as the product of the likelihood terms describing the $N_{exp,l}$ observations performed with

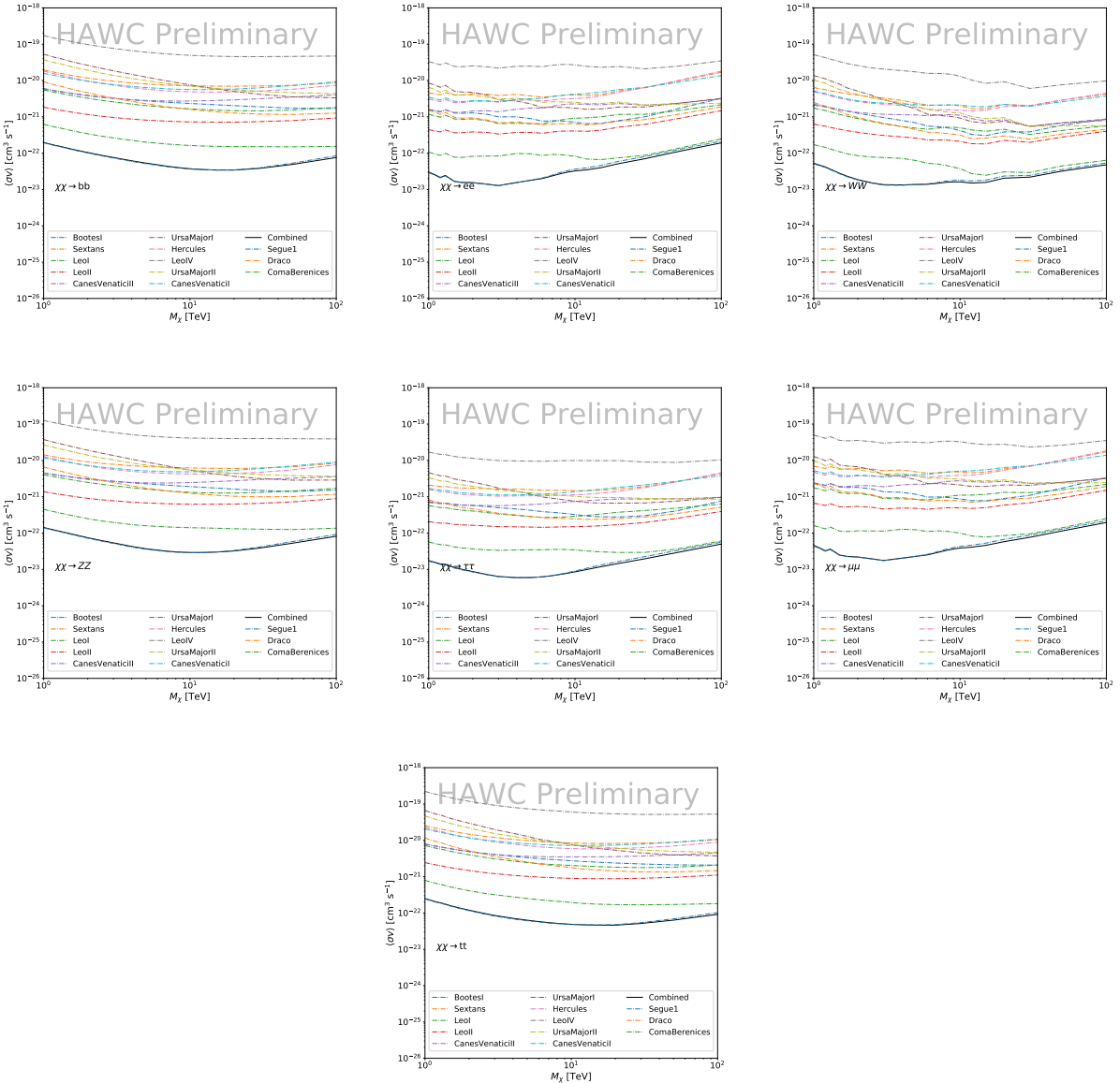


Figure 7.5 HAWC upper limits at 95% confidence level on $\langle\sigma v\rangle$ versus DM mass for seven annihilation channels, using the set of J -factors from Ref. [47]. The solid line represents the observed combined limit. Dashed lines represent limits from individual dSphs.

793 any of our observatories:

$$\mathcal{L}_{dSph,l} (\langle\sigma v\rangle; J_l, \nu_l | \mathcal{D}_l) = \prod_{k=1}^{N_{exp,l}} \mathcal{L}_{lk} (\langle\sigma v\rangle; J_l, \nu_{lk} | \mathcal{D}_{lk}), \quad (7.11)$$

794 where each \mathcal{L}_{lk} term refers to an observation of the l -th dSph with associated k -th instrument
 795 responses. $N_{exp,l}$ varies from dSph to dSph and can be retrieved from Tab. 7.2.

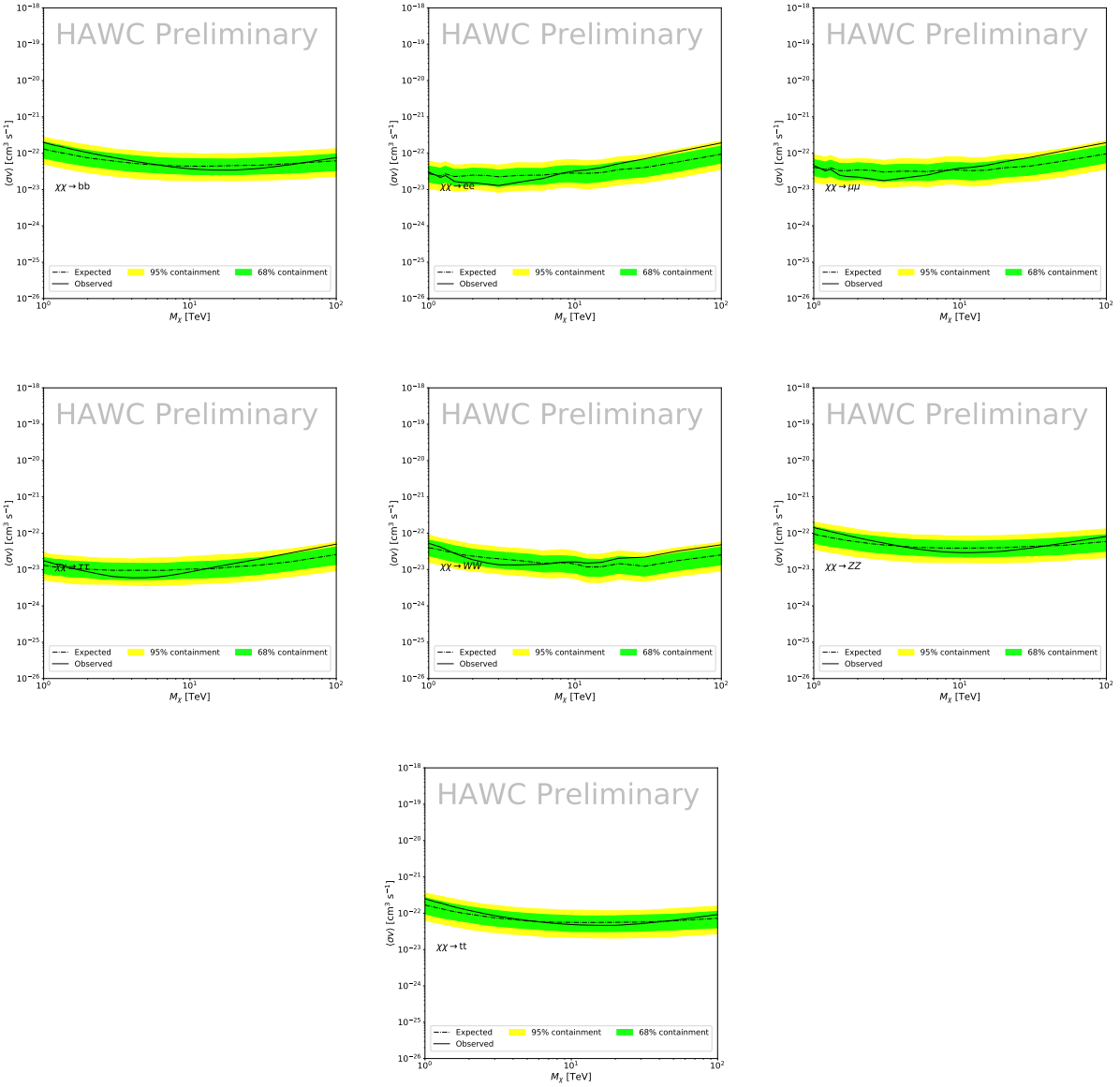


Figure 7.6 HAWC Brazil bands at 95% confidence level on $\langle\sigma v\rangle$ versus DM mass for seven annihilation channels with J -factors from \mathcal{GS} [47]. The solid line represents the combined limit from 13 dSphs. The dashed line is the expected limit. The green band is the 68% containment. The yellow band is the 95% containment.

796 No significant DM emission was observed by any of the five telescopes. We present upper
 797 limits on $\langle\sigma v\rangle$ using the test statistics, Eq. (7.10).

$$TS = -2 \ln \lambda(\langle\sigma v\rangle), \quad (7.12)$$

798 No significant DM emission was observed by any of the five instruments. We present the upper

799 limits on $\langle\sigma v\rangle$ assuming seven independent DM self annihilation channels, namely W^+W^- , Z^+Z^- ,
800 $b\bar{b}$, $t\bar{t}$, e^+e^- , $\mu^+\mu^-$, and $\tau^+\tau^-$. The 68% and 95% containment bands are produced from 300
801 Poisson realizations of the null hypothesis corresponding to each of the combined datasets. These
802 300 realizations are combined identically to dSph observations. The containment bands and the
803 median are extracted from the distribution of resulting limits on the null hypothesis. These 300
804 realizations are obtained either by fast simulations of the OFF observations, for H.E.S.S., MAGIC,
805 VERITAS, and HAWC, or taken from real observations of empty fields of view in the case of
806 Fermi-LAT [48, 49, 50].

807 The obtained limits are shown in Figure 7.7 for the \mathcal{GS} set of J -factors [47] and in Figure 7.8
808 for the \mathcal{B} set of J -factors [46, 51]. The combined limits are presented with their 68% and 95%
809 containment bands, and are expected to be close to the median limit when no signal is present.
810 We observe agreement with the null hypothesis for all channels, within 2σ standard deviations,
811 between the observed limits and the expectations given by the median limits. Limits obtained from
812 each detector are also indicated in the figures, where limits for all dSphs observed by the specific
813 instrument have been combined.

814 Below ~ 300 GeV, the *Fermi*-LAT dominates the DM limits for all annihilation channels. From
815 ~ 300 GeV to ~ 2 TeV, *Fermi*-LAT continues to dominate for the hadronic and bosonic DM channels,
816 yet the IACTs (H.E.S.S., MAGIC, and VERITAS) and *Fermi*-LAT all contribute to the limit for
817 leptonic DM channels. For DM masses between ~ 2 TeV to ~ 10 TeV, the IACTs dominate leptonic
818 DM annihilation channels, whereas both the *Fermi*-LAT and the IACTs dominate bosonic and
819 hadronic DM annihilation channels. From ~ 10 TeV to ~ 100 TeV, both the IACTs and HAWC
820 contribute significantly to the leptonic DM limit. For hadronic and bosonic DM, the IACTs and
821 *Fermi*-LAT both contribute strongly.

822 We notice that the limits computed using the \mathcal{B} set of J -factor are always better compared to the
823 ones calculated with the \mathcal{GS} set. For the W^+W^- , Z^+Z^- , $b\bar{b}$, and $t\bar{t}$ channels, the ratio between the
824 limits computed with the two sets of J -factor is varying between a factor of ~ 3 and ~ 5 depending
825 on the energy, with the largest ratio around 10 TeV. For the channels e^+e^- , $\mu^+\mu^-$, and $\tau^+\tau^-$, the

ratio lies between ~ 2 to ~ 6 , being maximum around 1 TeV. Examining Figure 7.15 and Figure 7.16 in Section 7.7, these differences are explained by the fact that the \mathcal{B} set provides higher J -factors for the majority of the studied dSphs, with the notable exception of Segue I. The variation on the ratio of the limits for the two sets is due to different dSph dominating the limits depending on the energy. This pushes the range of thermal cross-section which can be excluded to higher mass. This comparison demonstrates the magnitude of systematic uncertainties associated with the choice of the J -factor

This comparison demonstrates the magnitude of systematic uncertainties associated with the choice of the J -factor calculation. The \mathcal{GS} and \mathcal{B} sets present a difference in the limits for all channels of about This difference is explained, see Figure 7.15 and Figure 7.16 in Appendix, by the fact that the \mathcal{B} set provides higher J factors for all dSph except for Segue I. This pushes the range of thermal cross-section which can be excluded to higher mass.

7.6 HAWC Systematics

7.6.1 Inverse Compton Scattering

The DM-DM annihilation channels produce many high energy electrons regardless of the primary annihilation channel. These high energy electrons can produce high energy gamma-rays through Inverse Compton Scattering (ICS). If this effect is strong, it would change the morphology of the source and increase the total expected gamma-ray counts from any source. The PPPC [43] provides tools in Mathematica for calculating the impact of ICS for an arbitrary location in the sky for a specified annihilation channel. We calculated the change in gamma-ray counts for DM annihilation to primary $e\bar{e}$ for RA and Dec corresponding to Segue1 and Coma Berenices. These dSphs were chosen because they are the strongest contributors to the limit. $e\bar{e}$ was selected because it would have the largest number of high energy electrons. The effect was found to be on the order of 10^{-7} on the gamma-ray spectrum. As a result, this systematic is not considered in our analysis.

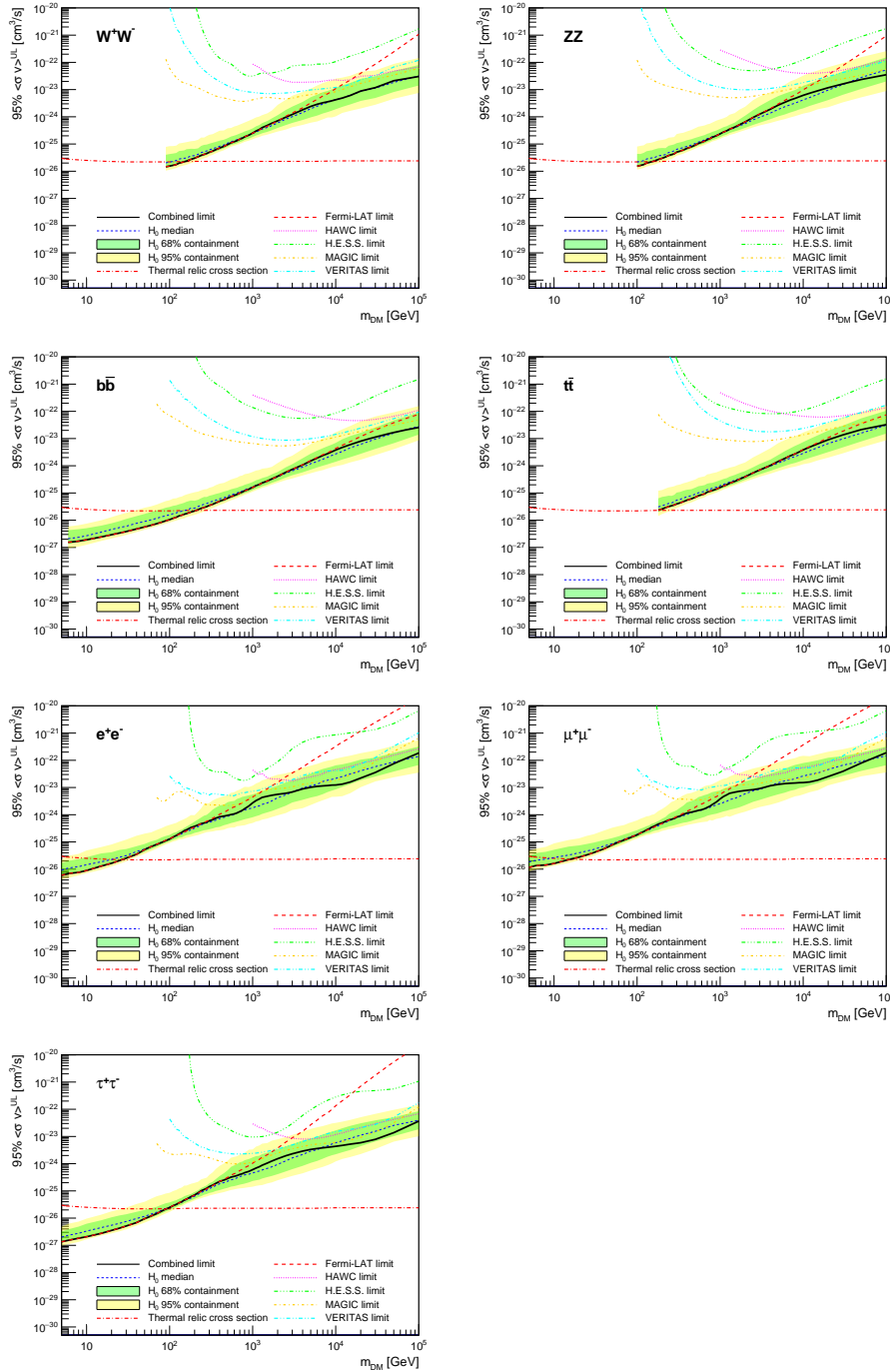


Figure 7.7 Upper limits at 95% confidence level on $\langle\sigma v\rangle$ in function of the DM mass for eight annihilation channels, using the set of J factors from Ref. [47] (\mathcal{GS} set in Table 7.1). The black solid line represents the observed combined limit, the black dashed line is the median of the null hypothesis corresponding to the expected limit, while the green and yellow bands show the 68% and 95% containment bands. Combined upper limits for each individual detector are also indicated as solid, colored lines. The value of the thermal relic cross-section in function of the DM mass is given as the red dotted-dashed line [52].

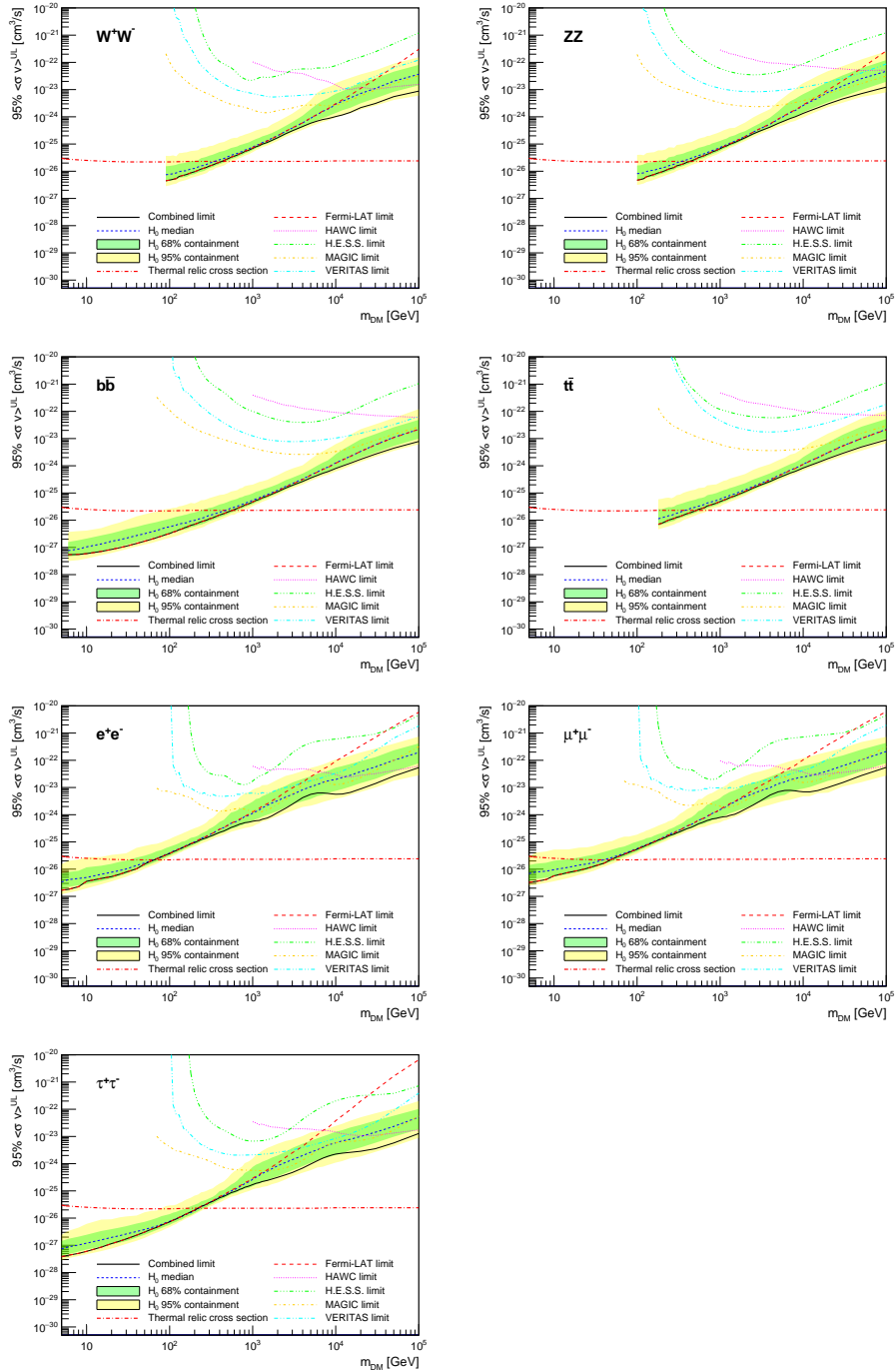


Figure 7.8 Same as Fig. 7.7, using the set of J factors from Ref. [46, 51] (\mathcal{B} set in Table 7.1).

7.6.2 Point Source Versus Extended Source Limits

The previous DM search toward dSph approximated the dSphs as point sources [45]. In this analysis, the dSphs are implemented as extended with J-factor distributions following those produced by [47]. The resolution of the cited map is much finer than HAWC's angular resolution.

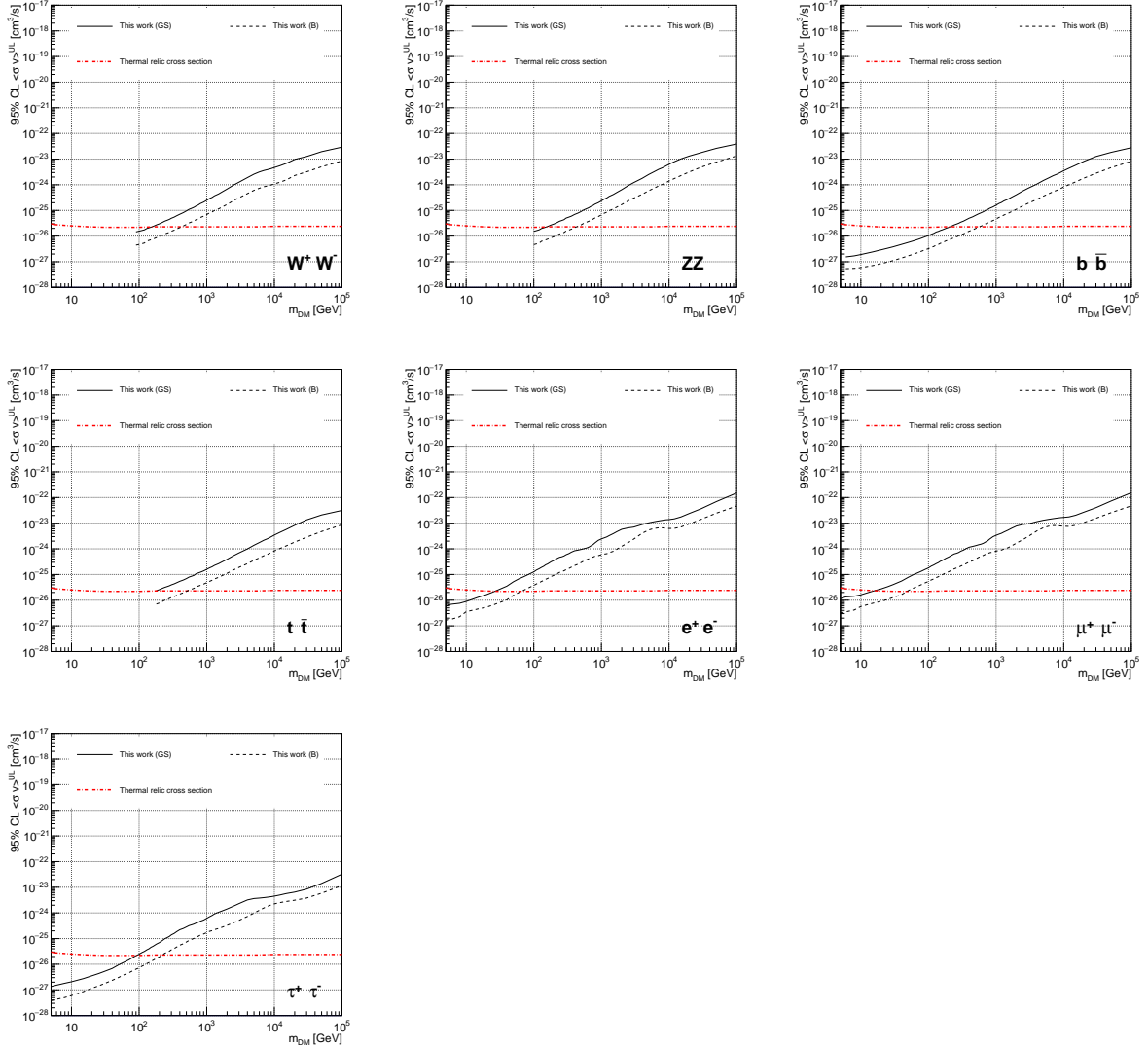


Figure 7.9 Comparisons of the combined limits at 95% confidence level for each of the eight annihilation channels when using the J factors from Ref. [47] (\mathcal{GS} set in Table 7.1), plain lines, and the J factor from Ref. [46, 51] (\mathcal{B} set in Table 7.1), dashed lines. The cross-section given by the thermal relic is also indicated [52].

854 The vast majority of the J-factor distribution is represented on the central HAWC pixel of the dSph
 855 spatial map. However, the neighboring 8 pixels are not negligible and contribute to our limit.

856 Figure 7.10 shows a substantial improvement to the limit for Segue1. Fig. 7.11 however showed
 857 identical limits. These disparities are best explained by the relative difference in their J-Factors.
 858 Both dSphs pass almost overhead the HAWC detector, however Segue1 has the larger J-Factor
 859 between the two. Adjacent pixels to the central pixel will therefore contribute to the limits. This is

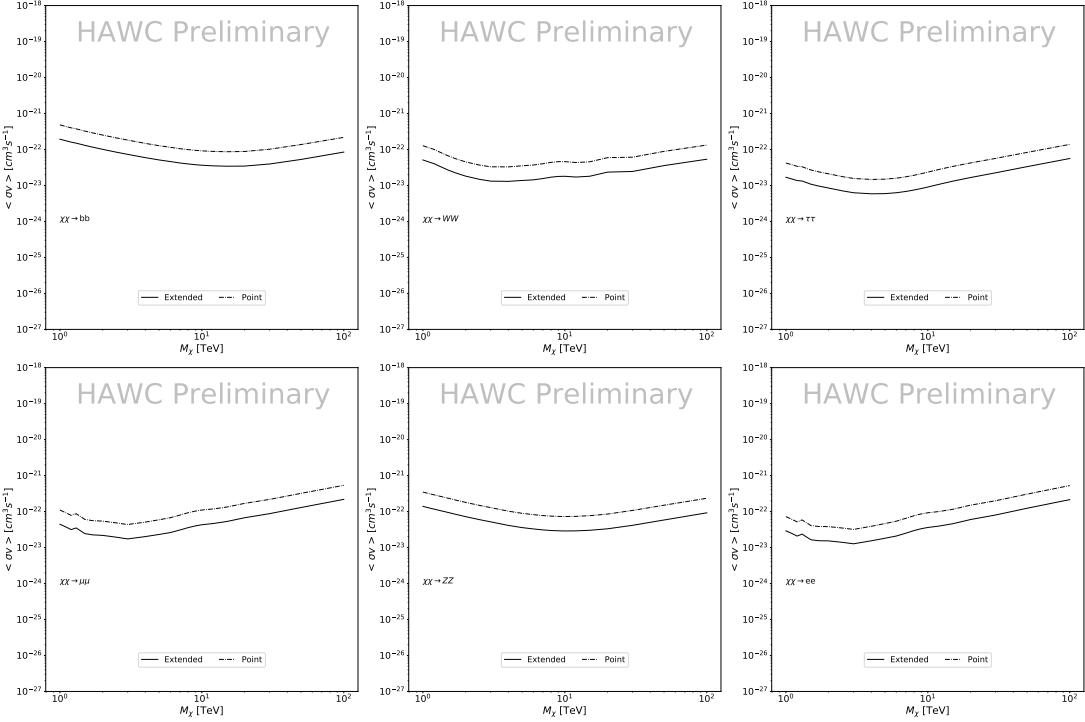


Figure 7.10 Comparisons of the combined limits at 95% confidence level for a point source analysis and extended source using [47] *GS* J-factor distributions and PPPC [43] annihilation spectra. Shown are the limits for Segue1 which will have the most significant impact on the combined limit. 6 of the 7 DM annihilation channels are shown. Solid lines are extended source studies. Dashed lines are point source studies. Overall, the extended source analysis improves the limit by a factor of 2.

860 the case for other dSph that are closer to overhead the HAWC detector.

861 Comparison plots for all sources and the combined limit can be found in the sandbox for the
862 Glory Duck project.

863 7.6.3 Impact of Pointing Systematic

864 During the analysis it was discovered that reconstruction of gamma-rays. Slides describing this
865 systematic can be found [here](#). Shown on the presentation is dependence on the pointing systematic
866 on declination. New spatial profiles were generated for every dSph and limits were computed for
867 the adjusted declination.

868 Section 7.6.3 demonstrates the impact of this systematic for all DM annihilation channels
869 studied by HAWC. The impact is a tiny improvement, yet mostly identical, to the combined limits.

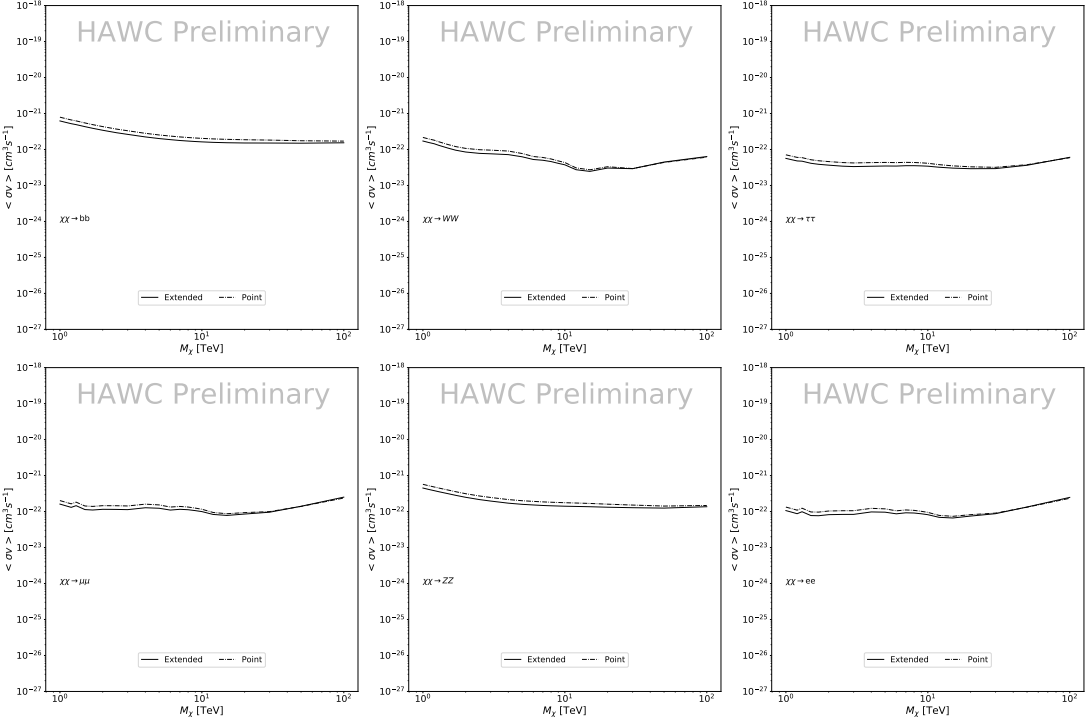


Figure 7.11 Same as Fig. 7.10 on Coma Berenices. This dSph also contributes significantly to the limit. The limits are identical in this case.

870 7.7 J-factor distributions

871 7.7.1 Numerical integration of \mathcal{GS} maps

872 It was discovered well after the HAWC analysis was completed that the published tables from
 873 \mathcal{GS} [44] quoted median J -factors were computed in a non-trivial manner. The assumption myself
 874 and collaborators had was that the published tables represented the J -factor as a function of θ for
 875 the best global fit model on a per source basis. However, this is not the case. Instead, what is
 876 published are the best fit model for each dwarf that only considers stars up to the angular separation
 877 θ . Therefore, the model is changing for each value of θ for each dwarf. Yet, the introduced features
 878 from unique models at each θ are much smaller than the angular resolution of HAWC. It is not
 879 expected for these effects to impact the limits and TS greatly as a result.

880 Median J -factor model profiles were provided by the authors. New maps were generated
 881 and analyzed for Segue1 and Coma Berenices. Figure 7.13 shows the differential between maps
 882 generated with the method from Section 7.7.1 and from the authors of [44]. These maps were

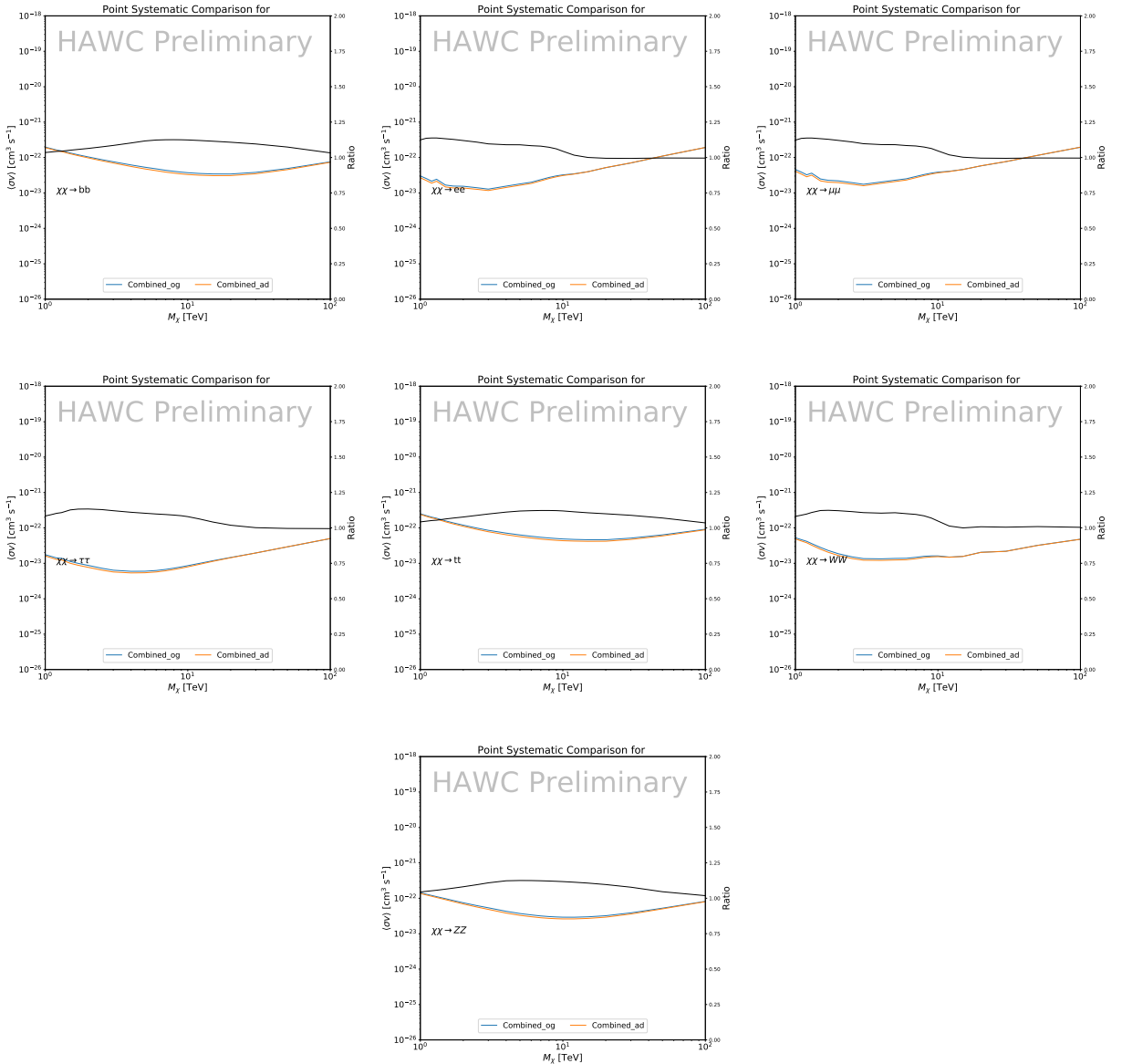


Figure 7.12 Comparison of combined limits when correcting for HAWC's pointing systematic. All DM annihilation channels are shown. The solid black line is the ratio between published limit to the declination corrected limit. The blue solid line or "Combined_og" represented the limits computed for Glory Duck. The solid orange line or "Combined_ad" represented the limits computed after correcting for the pointing systematic.

883 reanalyzed for all SM DM annihilation channels. Upper limits for these channels are shown in

884 Figure 7.14

885 From Figure 7.14, we can see that the impact of these model difference was no substantial.

886 The observed impact was a fractional effect which is much smaller than the impact from selecting

887 another DM spatial distribution model as was shown in Figure 7.9.

888 **7.7.2 \mathcal{GS} versus \mathcal{B} spatial models**

889 We show in this appendix a comparison between the J -factors computed by Geringer-Sameth
890 *et al.* [47] (the \mathcal{GS} set) and the ones computed by Bonnivard *et al.* [46, 51] (the \mathcal{B} set). The
891 \mathcal{GS} J -factors are computed through a Jeans analysis of the kinematic stellar data of the selected
892 dSphs, assuming a dynamic equilibrium and a spherical symmetry for the dSphs. They adopted
893 the generalized DM density distribution, known as Zhao-Hernquist, introduced by [53], carrying
894 three additional index parameters to describe the inner and outer slopes, and the break of the
895 density profile. Such a profile parametrization allows the reduction of the theoretical bias from
896 the choice of a specific radial dependency on the kinematic data. In other words, the increase of
897 free parameters with the use of the Zhao-Hernquist profile allows a better description of the mass
898 density distribution of dark matter.

899 In addition, a constant velocity anisotropy profile and a Plummer light profile [54] for the stellar
900 distribution were assumed. The velocity anisotropy profile depends on the radial and tangential
901 velocity dispersions. However, its determination remains challenging since only the line-of-sight
902 velocity dispersion can be derived from velocity measurements. Therefore, the parametrization of
903 the anisotropy profile is obtained from simulated halos (see [55] for more details). They provide the
904 values of the J -factors of regions extending to various angular radius up to the outermost member
905 star.

906 The \mathcal{B} J -factors were computed through a Jeans analysis taking into account the systematic
907 uncertainties induced by the DM profile parametrization, the radial velocity anisotropy profile, and
908 the triaxiality of the halo of the dwarf galaxies. They performed a more complete study of the dSph
909 kinematics and dynamics than \mathcal{GS} for the determination of the J -factor. Conservative values of the
910 J -factors where obtained using an Einasto DM density profile [56], a realistic anisotropy profile
911 known as the Baes & Van Hese profile [57] which takes into account that the inner regions can be
912 significantly non-isotropic, and a Zhao-Hernquist light profile [53].

913 For both sets, J -factor values are provided for all dSphs as a function of the radius of the

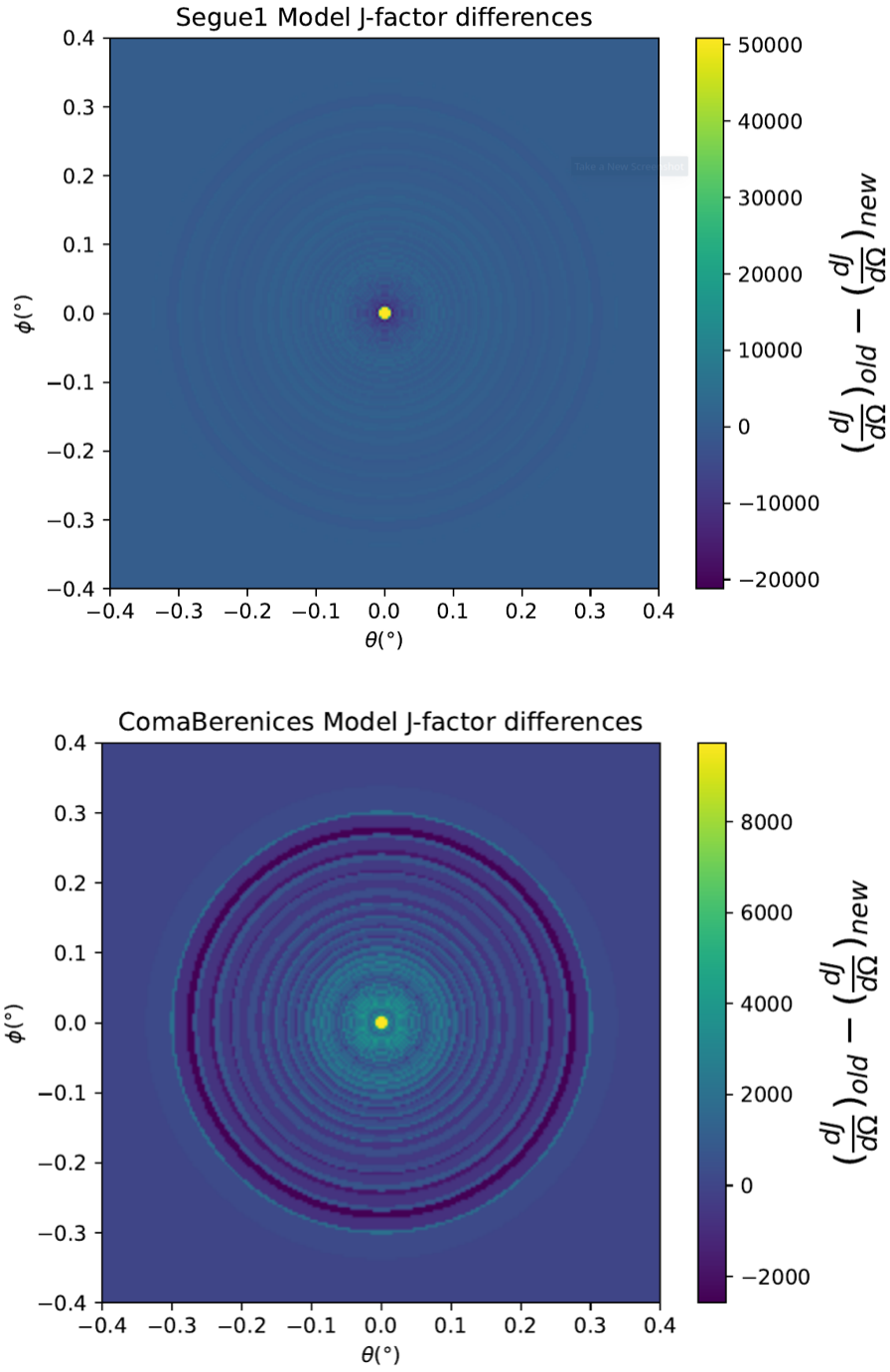


Figure 7.13 Differential map of dJ/Ω from model built in Section 7.7.1 and profiles provided directly from authors. (Top) Differential from Segue1. (bottom) Differential from Coma Berenices. Note that their scales are not the same. Segue1 shows the deepest discrepancies which is congruent with its large uncertainties. Both models show anuli where unique models become apparent.

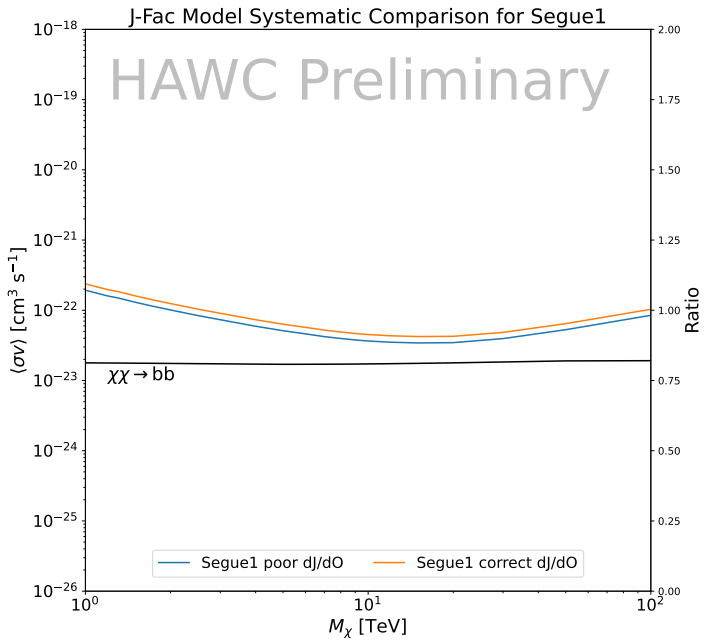
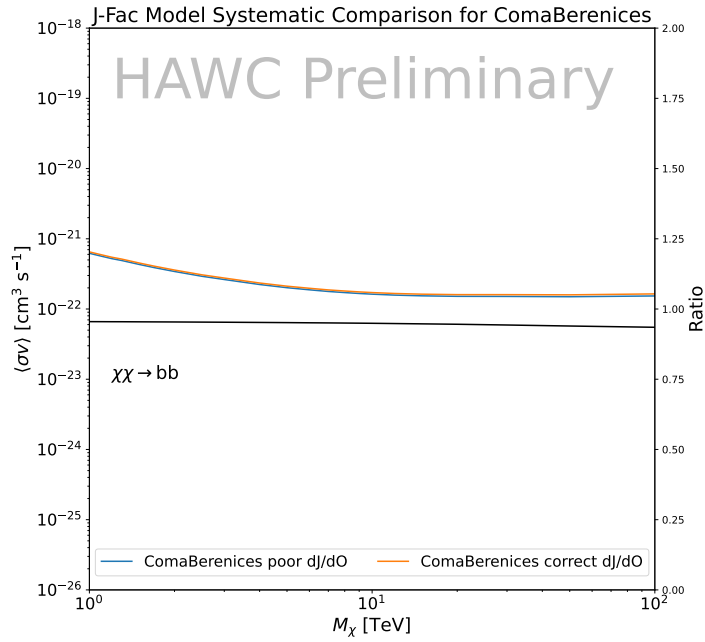


Figure 7.14 HAWC limits for Coma Berenices (top) and Segue1 (bottom) for two different map sets. Blue lines are limits calculated on maps with poor model representation. Orange lines are limits calculated on spatial profiles provided by the authors of [44]. Black line is the ratio of the poor spatial model limits to the corrected spatial models. The left y-axis measures $\langle \sigma v \rangle$ for the blue and orange lines. The right y-axis measures the ratio and is unitless.

914 integration region [47, 46, 51]. Table 7.1 shows the heliocentric distance and Galactic coordinates
915 of the twenty dSphs, together with the two sets of J -factor values integrated up to the outermost
916 observed star for \mathcal{GS} and the tidal radius for \mathcal{B} . Both J -factor sets were derived through a Jeans
917 analysis based on the same kinematic data, except for Draco where the measurements of [58] have
918 been adopted in the computation of the \mathcal{B} value. The computations for producing the \mathcal{GS} and \mathcal{B}
919 samples differ in the choice of the DM density, velocity anisotropy, and light profiles, for which the
920 set \mathcal{B} takes into account some sources of systematic uncertainties.

921 Figure 7.15 and Figure 7.16 show the comparisons for the J -factor versus the angular radius
922 for each of the 20 dSphs used in this study. The uncertainties provided by the authors are also
923 indicated in the figures. For the \mathcal{GS} set, the computation stops at the angular radius corresponding
924 to the outermost observed star, while for the \mathcal{B} set, the computation stops at the angular radius
925 corresponding to the tidal radius.

926 7.8 Discussion and Conclusions

927 In this multi-instrument analysis, we have used observations of 20 dSphs from the gamma-ray
928 telescopes Fermi-LAT, H.E.S.S., MAGIC, VERITAS, and HAWC to perform a collective DM
929 search annihilation signals. The data were combined across sources and detectors to significantly
930 increase the sensitivity of the search. We have observed no significant deviation from the null, no
931 DM, hypothesis, and so present our results in terms of upper limits on the annihilation cross section
932 for seven potential DM annihilation channels.

933 Fermi-LAT brings the most stringent constraints for continuum channels below approximately
934 1 TeV. the remaining detectors dominate at higher energies. Overall, for multi-TeV DM mass,
935 the combined DM constraints from all five telescopes are 2-3 times stronger than any individual
936 telescope for multi-TeV DM.

937 Derived from observations of many dSphs, our results produce robust limits given the DM
938 content of the dSphs is relatively well constrained. The obtained limits span the largest mass
939 range of any WIMP DM search. Our combined analysis improves the sensitivity over previously
940 published results from each detectors which produces the most stringent limits on DM annihilation

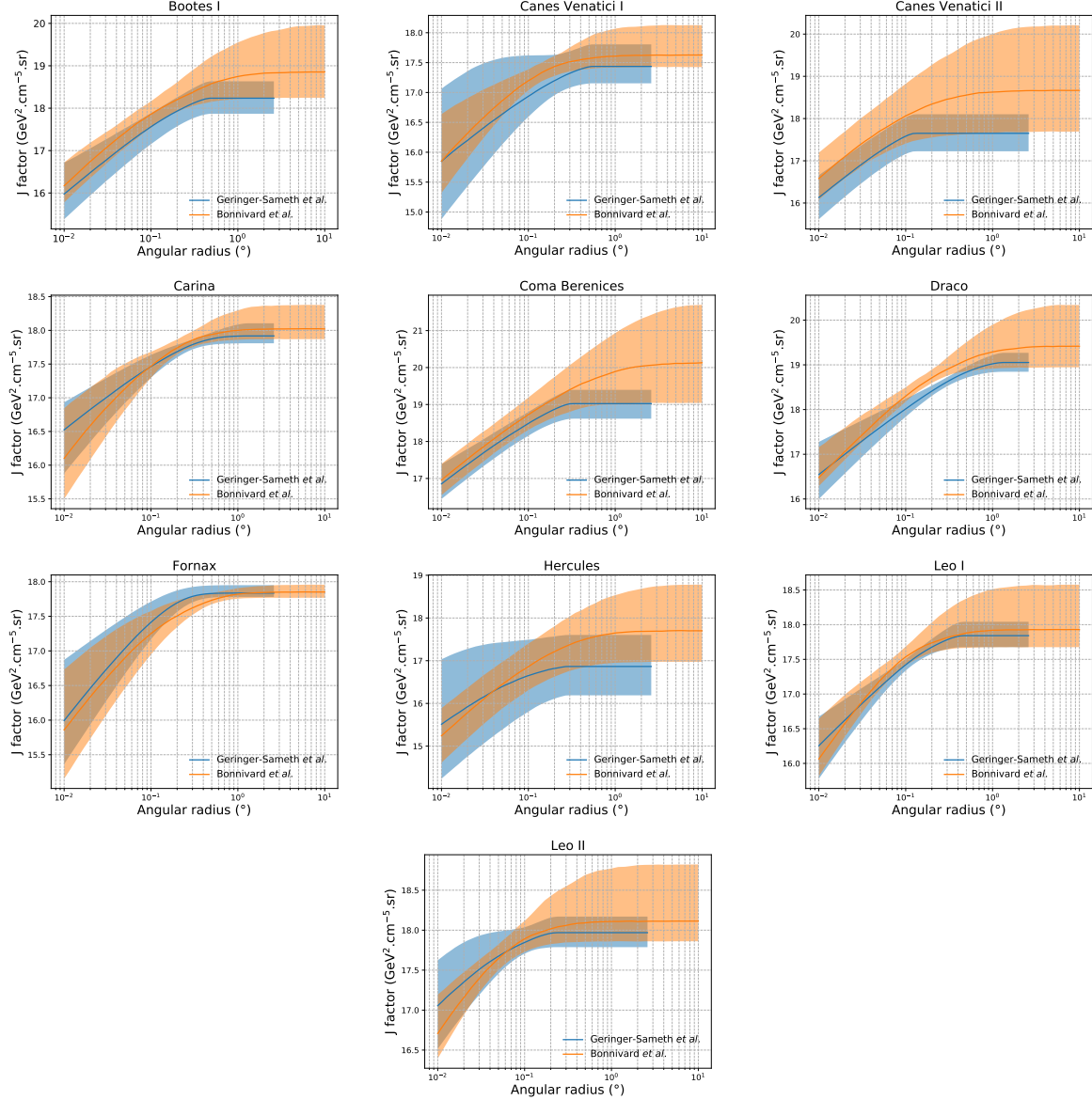


Figure 7.15 Comparisons between the J -factors versus the angular radius for the computation of J factors from Ref. [47] (\mathcal{GS} set in Table 7.1) in blue and for the computation from Ref. [46, 51] (\mathcal{B} set in Tab. 7.1) in orange. The solid lines represent the central value of the J -factors while the shaded regions correspond to the 1σ standard deviation.

from dSphs. These results are based on deep exposures of the most promising known dSphs with the currently most sensitive gamma-ray instruments. Therefore, our results constitute a legacy of a generation of gamma-ray instruments on WIMP DM searches towards dSphs. Our results will remain the reference in the field until a new generation of more sensitive gamma-ray instruments begin operations, or until new dSphs with higher J -factors are discovered.

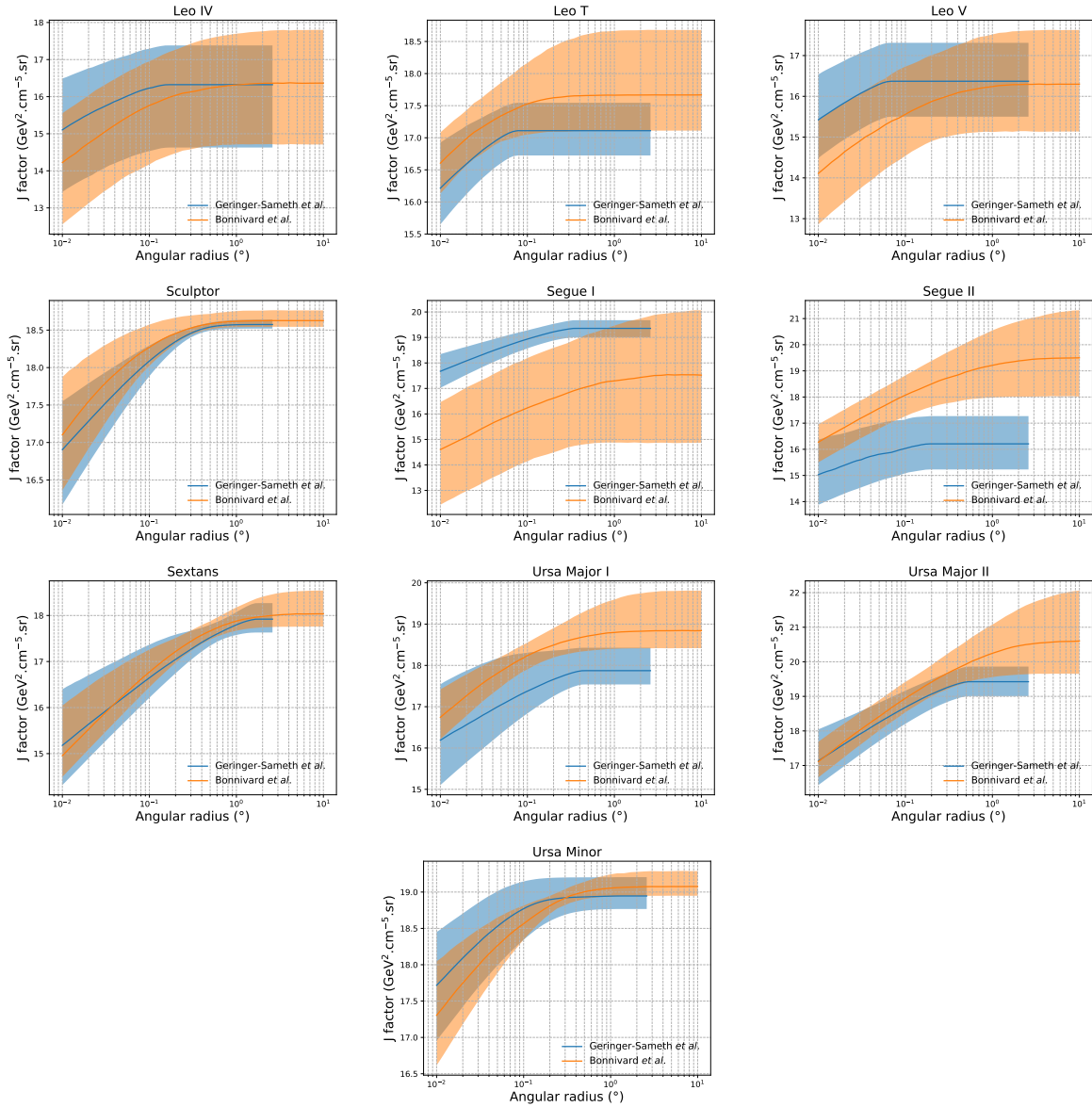


Figure 7.16 Comparisons between the J -factors versus the angular radius for the computation of J factors from Ref. [47] (\mathcal{GS} set in Tab. 7.1) in blue and for the computation from Ref. [46, 51] (\mathcal{B} set in Tab. 7.1) in orange. The solid lines represent the central value of the J -factors while the shaded regions correspond to the 1σ standard deviation.

946 This analysis serves as a proof of concept for future multi-instrument and multi-messenger
 947 combination analyses. With this collaborative effort, we have managed to sample over four orders
 948 in magnitude in gamma-ray energies with distinct observational techniques. Determining the nature
 949 of DM continues to be an elusive and difficult problem. Larger datasets with diverse measurement
 950 techniques could be essential to tackling the DM problem. A future collaboration using similar

951 techniques as the ones described in this paper could grow even beyond gamma rays. The models we
952 used for this study include annihilation channels with neutrinos in the final state. Advanced studies
953 could aim to merge our results with those from neutrino observatories with large data sets. Efforts
954 are already underway to add data from the IceCube, ANTARES, and KM3NeT observatories to
955 these gamma-ray results.

956 From this work, a selection of the best candidates for observations, according to the latest
957 knowledge on stellar dynamics and modelling techniques for the derivation of the J -factors on the
958 potential dSphs targets, is highly desirable at the time that new experiments are starting their dark
959 matter programmes using dSphs. Given the systematic uncertainty inherent to the derivation of
960 the J -factors, an informed observational strategy would be to select both objects with the highest
961 J -factors that could lead to DM signal detection, and objects with robust J -factor predictions, i.e.
962 with kinematic measurements on many bright stars, which would strengthen the DM interpretation
963 reliability of the observation outcome.

964 This analysis combines data from multiple telescopes to produce strong constraints on astro-
965 physical objects. From this perspective, these methods can be applied beyond just DM searches.
966 Almost every astrophysical study can benefit from multi-telescope, multi-wavelength gamma-ray
967 studies. We have enabled these telescopes to study the cosmos with greater precision and detail.
968 Many astrophysical searches can benefit from multi-instrument gamma-ray studies, for which our
969 analysis lays the foundation.

970

CHAPTER 8

NU DUCK

CHAPTER 9

MULTITHREADING HAWC ANALYSES FOR DARK MATTER SEARCHES

BIBLIOGRAPHY

- 973 [1] Anne M. Green. “Dark matter in astrophysics/cosmology”. In: *SciPost Phys. Lect.*
 974 *Notes* (2022), p. 37. doi: [10.21468/SciPostPhysLectNotes.37](https://doi.org/10.21468/SciPostPhysLectNotes.37). URL: <https://scipost.org/10.21468/SciPostPhysLectNotes.37>.
- 976 [2] Bing-Lin Young. “A survey of dark matter and related topics in cosmology”. In: *Frontiers*
 977 *of Physics* 12 (Oct. 2016). doi: <https://doi.org/10.1007/s11467-016-0583-4>.
 978 URL: <https://doi.org/10.1007/s11467-016-0583-4>.
- 979 [3] Gianfranco Bertone, Dan Hooper, and Joseph Silk. “Particle dark matter: evidence,
 980 candidates and constraints”. In: *Physics Reports* 405.5 (2005), pp. 279–390. ISSN:
 981 0370-1573. doi: <https://doi.org/10.1016/j.physrep.2004.08.031>. URL:
 982 <https://www.sciencedirect.com/science/article/pii/S0370157304003515>.
- 983 [4] Gianfranco Bertone and Dan Hooper. “History of dark matter”. In: *Rev. Mod. Phys.*
 984 90 (4 Aug. 2018), p. 045002. doi: [10.1103/RevModPhys.90.045002](https://doi.org/10.1103/RevModPhys.90.045002). URL: <https://link.aps.org/doi/10.1103/RevModPhys.90.045002>.
- 986 [5] Fritz Zwicky. “The Redshift of Extragalactic Nebulae”. In: *Helvetica Physica Acta* 6.
 987 (1933), pp. 110–127. doi: [10.5169/seals-110267](https://doi.org/10.5169/seals-110267).
- 988 [6] Vera C. Rubin and Jr. Ford W. Kent. “Rotation of the Andromeda Nebula from a
 989 Spectroscopic Survey of Emission Regions”. In: *ApJ* 159 (Feb. 1970), p. 379. doi:
 990 [10.1086/150317](https://doi.org/10.1086/150317).
- 991 [7] K. G. Begeman, A. H. Broeils, and R. H. Sanders. “Extended rotation curves of spiral galax-
 992 ies: dark haloes and modified dynamics”. In: *Monthly Notices of the Royal Astronomical So-*
 993 *ciety* 249.3 (Apr. 1991), pp. 523–537. ISSN: 0035-8711. doi: [10.1093/mnras/249.3.523](https://doi.org/10.1093/mnras/249.3.523).
 994 eprint: <https://academic.oup.com/mnras/article-pdf/249/3/523/18160929/mnras249-0523.pdf>. URL: <https://doi.org/10.1093/mnras/249.3.523>.
- 996 [8] *Different types of gravitational lenses*. website. Feb. 2004. URL: <https://esahubble.org/images/heic0404b/>.
- 998 [9] Douglas Clowe et al. “A Direct Empirical Proof of the Existence of Dark Matter”. In: *apjl*
 999 648.2 (Sept. 2006), pp. L109–L113. doi: [10.1086/508162](https://doi.org/10.1086/508162). arXiv: [astro-ph/0608407](https://arxiv.org/abs/astro-ph/0608407)
 1000 [[astro-ph](https://arxiv.org/abs/astro-ph/0608407)].
- 1001 [10] Planck Collaboration and N. et. al. Aghanim. “Planck 2018 results I. Overview and the
 1002 cosmological legacy of Planck”. In: *A&A* 641 (2020). doi: [10.1051/0004-6361/201833880](https://doi.org/10.1051/0004-6361/201833880). URL: <https://doi.org/10.1051/0004-6361/201833880>.
- 1004 [11] Wayne Hu. *Matter Density Animation*. web. 2024. URL: <http://background.uchicago.edu/~whu/animbut/anim2.html>.

- 1006 [12] Wenlong Yuan et al. “A First Look at Cepheids in a Type Ia Supernova Host with JWST”. in:
1007 *The Astrophysical Journal Letters* 940.1 (Nov. 2022). doi: [10.3847/2041-8213/ac9b27](https://doi.org/10.3847/2041-8213/ac9b27).
1008 URL: <https://dx.doi.org/10.3847/2041-8213/ac9b27>.
- 1009 [13] Wendy L. Freedman. “Measurements of the Hubble Constant: Tensions in Perspective”. In:
1010 *The Astrophysical Journal* 919.1 (Sept. 2021), p. 16. doi: [10.3847/1538-4357/ac0e95](https://doi.org/10.3847/1538-4357/ac0e95).
1011 URL: <https://dx.doi.org/10.3847/1538-4357/ac0e95>.
- 1012 [14] Jodi Cooley. “Dark Matter direct detection of classical WIMPs”. In: *SciPost Phys. Lect.
1013 Notes* (2022), p. 55. doi: [10.21468/SciPostPhysLectNotes.55](https://doi.org/10.21468/SciPostPhysLectNotes.55). URL: <https://scipost.org/10.21468/SciPostPhysLectNotes.55>.
- 1015 [15] “Search for new phenomena in events with an energetic jet and missing transverse momentum
1016 in pp collisions at $\sqrt{s} = 13$ TeV with the ATLAS detector”. In: *Phys. Rev. D* 103
1017 (11 July 2021), p. 112006. doi: [10.1103/PhysRevD.103.112006](https://doi.org/10.1103/PhysRevD.103.112006). URL: <https://link.aps.org/doi/10.1103/PhysRevD.103.112006>.
- 1019 [16] *Jetting into the dark side: a precision search for dark matter*. website. July 2020. URL:
1020 <https://atlas.cern/updates/briefing/precision-search-dark-matter>.
- 1021 [17] Celine Armand et. al. “Combined dark matter searches towards dwarf spheroidal galaxies
1022 with Fermi-LAT, HAWC, H.E.S.S., MAGIC, and VERITAS”. in: *Proceedings of Science*.
1023 Vol. 395. Mar. 2022. doi: <https://doi.org/10.22323/1.395.0528>.
- 1024 [18] Tracy R. Slatyer. “Les Houches Lectures on Indirect Detection of Dark Matter”. In: *SciPost
1025 Phys. Lect. Notes* (2022), p. 53. doi: [10.21468/SciPostPhysLectNotes.53](https://doi.org/10.21468/SciPostPhysLectNotes.53). URL:
1026 <https://scipost.org/10.21468/SciPostPhysLectNotes.53>.
- 1027 [19] Christian W Bauer, Nicholas L. Rodd, and Bryan R. Webber. “Dark matter spectra from
1028 the electroweak to the Planck scale”. In: *Journal of High Energy Physics* 2021.1029-8479
1029 (June 2021). doi: [https://doi.org/10.1007/JHEP06\(2021\)121](https://doi.org/10.1007/JHEP06(2021)121).
- 1030 [20] Riccardo Catena and Piero Ullio. “A novel determination of the local dark matter density”.
1031 In: *Journal of Cosmology and Astroparticle Physics* 2010.08 (Aug. 2010), p. 004. doi:
1032 [10.1088/1475-7516/2010/08/004](https://doi.org/10.1088/1475-7516/2010/08/004). URL: <https://dx.doi.org/10.1088/1475-7516/2010/08/004>.
- 1034 [21] B. P. Abbott et al. “Observation of Gravitational Waves from a Binary Black Hole Merger”.
1035 In: *Phys. Rev. Lett.* 116 (6 Feb. 2016), p. 061102. doi: [10.1103/PhysRevLett.116.061102](https://doi.org/10.1103/PhysRevLett.116.061102). URL: <https://link.aps.org/doi/10.1103/PhysRevLett.116.061102>.
- 1037 [22] R. Abbasi et. al. “Observation of high-energy neutrinos from the Galactic plane”. In: *Science*
1038 380.6652 (June 2023), pp. 1338–1343.
- 1039 [23] NASA Goddard Space Flight Center. *Fermi’s 12-year view of the gamma-ray sky*. website.

- 1040 2022. URL: <https://svs.gsfc.nasa.gov/14090>.
- 1041 [24] Marco Cirelli et al. “PPPC 4 DM ID: a poor particle physicist cookbook for dark matter
1042 indirect detection”. In: *Journal of Cosmology and Astroparticle Physics* 2011.03 (Mar.
1043 2011), p. 051. doi: [10.1088/1475-7516/2011/03/051](https://doi.org/10.1088/1475-7516/2011/03/051). URL: <https://dx.doi.org/10.1088/1475-7516/2011/03/051>.
- 1044
- 1045 [25] W. B. Atwood et al. “The Large Area Telescope on the Fermi Gamma-Ray Space Telescope
1046 Mission”. In: *apj* 697.2 (June 2009), pp. 1071–1102. doi: [10.1088/0004-637X/697/2/1071](https://doi.org/10.1088/0004-637X/697/2/1071). arXiv: [0902.1089 \[astro-ph.IM\]](https://arxiv.org/abs/0902.1089).
- 1047
- 1048 [26] M. Ackermann et al. “Searching for Dark Matter Annihilation from Milky Way Dwarf
1049 Spheroidal Galaxies with Six Years of Fermi Large Area Telescope Data”. In: *prl* 115.23,
1050 231301 (Dec. 2015), p. 231301. doi: [10.1103/PhysRevLett.115.231301](https://doi.org/10.1103/PhysRevLett.115.231301). arXiv:
1051 [1503.02641 \[astro-ph.HE\]](https://arxiv.org/abs/1503.02641).
- 1052 [27] Mattia Di Mauro, Martin Stref, and Francesca Calore. “Investigating the effect of Milky
1053 Way dwarf spheroidal galaxies extension on dark matter searches with Fermi-LAT data”.
1054 In: *Phys. Rev. D* 106 (12 Dec. 2022), p. 123032. doi: [10.1103/PhysRevD.106.123032](https://doi.org/10.1103/PhysRevD.106.123032).
1055 URL: <https://link.aps.org/doi/10.1103/PhysRevD.106.123032>.
- 1056 [28] F. et al. Aharonian. “Observations of the Crab Nebula with H.E.S.S.”. In: *Astron. Astrophys.*
1057 457 (2006), pp. 899–915. doi: [10.1051/0004-6361:20065351](https://doi.org/10.1051/0004-6361:20065351). arXiv: [astro-ph/0607333](https://arxiv.org/abs/astro-ph/0607333).
- 1058
- 1059 [29] J. Albert et al. “VHE γ -Ray Observation of the Crab Nebula and its Pulsar with the MAGIC
1060 Telescope”. In: *The Astrophysical Journal* 674.2 (Feb. 2008), p. 1037. doi: [10.1086/525270](https://doi.org/10.1086/525270). URL: <https://dx.doi.org/10.1086/525270>.
- 1061
- 1062 [30] N. Park. “Performance of the VERITAS experiment”. In: *Proceedings, 34th International
1063 Cosmic Ray Conference (ICRC2015): The Hague, The Netherlands, July, 30th July - 6th
1064 August*. Vol. 34. 2015, p. 771. arXiv: [1508.07070 \[astro-ph.IM\]](https://arxiv.org/abs/1508.07070).
- 1065 [31] A. Abramowski et al. “H.E.S.S. constraints on Dark Matter annihilations towards the Sculptor
1066 and Carina Dwarf Galaxies”. In: *Astropart. Phys.* 34 (2011), pp. 608–616. doi: [10.1016/j.astropartphys.2010.12.006](https://doi.org/10.1016/j.astropartphys.2010.12.006). arXiv: [1012.5602 \[astro-ph.HE\]](https://arxiv.org/abs/1012.5602).
- 1067
- 1068 [32] A. Abramowski et al. “Search for dark matter annihilation signatures in H.E.S.S. observations
1069 of Dwarf Spheroidal Galaxies”. In: *Phys. Rev. D* 90 (2014), p. 112012. doi: [10.1103/PhysRevD.90.112012](https://doi.org/10.1103/PhysRevD.90.112012). arXiv: [1410.2589 \[astro-ph.HE\]](https://arxiv.org/abs/1410.2589).
- 1070
- 1071 [33] H. Abdalla et al. “Searches for gamma-ray lines and ‘pure WIMP’ spectra from Dark
1072 Matter annihilations in dwarf galaxies with H.E.S.S”. in: *JCAP* 11 (2018), p. 037. doi:
1073 [10.1088/1475-7516/2018/11/037](https://doi.org/10.1088/1475-7516/2018/11/037). arXiv: [1810.00995 \[astro-ph.HE\]](https://arxiv.org/abs/1810.00995).
- 1074

- 1074 [34] J. Aleksić et al. “Optimized dark matter searches in deep observations of Segue 1 with
1075 MAGIC”. in: *JCAP* 1402 (2014), p. 008. doi: [10.1088/1475-7516/2014/02/008](https://doi.org/10.1088/1475-7516/2014/02/008).
1076 arXiv: [1312.1535 \[hep-ph\]](https://arxiv.org/abs/1312.1535).
- 1077 [35] V.A. Acciari et al. “Combined searches for dark matter in dwarf spheroidal galaxies observed
1078 with the MAGIC telescopes, including new data from Coma Berenices and Draco”. In:
1079 *Physics of the Dark Universe* (2021), p. 100912. ISSN: 2212-6864. doi: <https://doi.org/10.1016/j.dark.2021.100912>. URL: <https://www.sciencedirect.com/science/article/pii/S2212686421001370>.
- 1082 [36] M. L. Ahnen et al. “Indirect dark matter searches in the dwarf satellite galaxy Ursa Major II
1083 with the MAGIC Telescopes”. In: *JCAP* 1803.03 (2018), p. 009. doi: [10.1088/1475-7516/2018/03/009](https://doi.org/10.1088/1475-7516/2018/03/009). arXiv: [1712.03095 \[astro-ph.HE\]](https://arxiv.org/abs/1712.03095).
- 1085 [37] S. et al. Archambault. “Dark matter constraints from a joint analysis of dwarf Spheroidal
1086 galaxy observations with VERITAS”. in: *prd* 95.8 (Apr. 2017). doi: [10.1103/PhysRevD.95.082001](https://doi.org/10.1103/PhysRevD.95.082001). arXiv: [1703.04937 \[astro-ph.HE\]](https://arxiv.org/abs/1703.04937).
- 1088 [38] Louise Oakes et al. “Combined Dark Matter searches towards dwarf spheroidal galaxies with
1089 Fermi-LAT, HAWC, HESS, MAGIC and VERITAS”. in: *Proceedings of Science*. 2019.
- 1090 [39] Celine Armand et al. on behalf of the Fermi-LAT, HAWC, HESS, MAGIC, VERITAS.
1091 “Combined Dark Matter searches towards dwarf spheroidal galaxies with Fermi-LAT,
1092 HAWC, HESS, MAGIC and VERITAS”. in: *Proceedings of Science*. 2021.
- 1093 [40] Daniel Kerszberg et al. on behalf of the Fermi-LAT, HAWC, HESS, MAGIC, and VER-
1094 TIAS collaborations. “Search for dark matter annihilation with a combined analysis of
1095 dwarf spheroidal galaxies from Fermi-LAT, HAWC, H.E.S.S., MAGIC and VERITAS”. in:
1096 *Proceedings of Science*. 2023.
- 1097 [41] A. U. Abeysekara et al. “Observation of the Crab Nebula with the HAWC Gamma-Ray
1098 Observatory”. In: *The Astrophysical Journal* 843.1 (June 2017), p. 39. doi: [10.3847/1538-4357/aa7555](https://doi.org/10.3847/1538-4357/aa7555). URL: <https://doi.org/10.3847/1538-4357/aa7555>.
- 1100 [42] Giacomo Vianello et al. *The Multi-Mission Maximum Likelihood framework (3ML)*. 2015.
1101 arXiv: [1507.08343 \[astro-ph.HE\]](https://arxiv.org/abs/1507.08343).
- 1102 [43] Marco Cirelli et al. “PPPC 4 DM ID: a poor particle physicist cookbook for dark matter
1103 indirect detection”. In: *Journal of Cosmology and Astroparticle Physics* 2011.03 (Mar.
1104 2011). ISSN: 1475-7516. doi: [10.1088/1475-7516/2011/03/051](https://doi.org/10.1088/1475-7516/2011/03/051). URL: <http://dx.doi.org/10.1088/1475-7516/2011/03/051>.
- 1106 [44] Alex Geringer-Sameth, Savvas M. Koushiappas, and Matthew Walker. “DWARF GALAXY
1107 ANNIHILATION AND DECAY EMISSION PROFILES FOR DARK MATTER EXPERI-
1108 MENTS”. in: *The Astrophysical Journal* 801.2 (Mar. 2015), p. 74. ISSN: 1538-4357. doi:

- 1109 10.1088/0004-637X/801/2/74. URL: <http://dx.doi.org/10.1088/0004-637X/80>
1110 1/2/74.
- 1111 [45] A. Albert et al. “Dark Matter Limits from Dwarf Spheroidal Galaxies with the HAWC
1112 Gamma-Ray Observatory”. In: *The Astrophysical Journal* 853.2 (Feb. 2018), p. 154. ISSN:
1113 1538-4357. doi: 10.3847/1538-4357/aaa6d8. URL: <http://dx.doi.org/10.3847/1538-4357/aaa6d8>.
- 1115 [46] V. Bonnivard et al. “Spherical Jeans analysis for dark matter indirect detection in dwarf
1116 spheroidal galaxies - Impact of physical parameters and triaxiality”. In: *Mon. Not. Roy.
1117 Astron. Soc.* 446 (2015), pp. 3002–3021. doi: 10.1093/mnras/stu2296. arXiv:
1118 1407.7822 [astro-ph.HE].
- 1119 [47] Alex Geringer-Sameth and Matthew Koushiappas Savvas M. and Walker. “Dwarf galaxy
1120 annihilation and decay emission profiles for dark matter experiments”. In: *Astrophys.
1121 J.* 801.2 (2015), p. 74. doi: 10.1088/0004-637X/801/2/74. arXiv: 1408.0002
1122 [astro-ph.CO].
- 1123 [48] M. Ackermann et al. “Searching for Dark Matter Annihilation from Milky Way Dwarf
1124 Spheroidal Galaxies with Six Years of Fermi Large Area Telescope Data”. In: *prl* 115.23,
1125 231301 (Dec. 2015), p. 231301. doi: 10.1103/PhysRevLett.115.231301. arXiv:
1126 1503.02641 [astro-ph.HE].
- 1127 [49] A. et al. Albert. “Searching for Dark Matter Annihilation in Recently Discovered Milky Way
1128 Satellites with Fermi-LAT”. in: *Astrophys. J.* 834.2 (2017), p. 110. doi: 10.3847/1538-4
1129 357/834/2/110. arXiv: 1611.03184 [astro-ph.HE].
- 1130 [50] Mattia Di Mauro and Martin Wolfgang Winkler. “Multimessenger constraints on the dark
1131 matter interpretation of the Fermi-LAT Galactic Center excess”. In: *prd* 103.12, 123005
1132 (June 2021), p. 123005. doi: 10.1103/PhysRevD.103.123005. arXiv: 2101.11027
1133 [astro-ph.HE].
- 1134 [51] V. Bonnivard et al. “Dark matter annihilation and decay in dwarf spheroidal galaxies: The
1135 classical and ultrafaint dSphs”. In: *Mon. Not. Roy. Astron. Soc.* 453.1 (2015), pp. 849–867.
1136 doi: 10.1093/mnras/stv1601. arXiv: 1504.02048 [astro-ph.HE].
- 1137 [52] Gianfranco Bertone, Dan Hooper, and Joseph Silk. “Particle dark matter: evidence, can-
1138 didates and constraints”. In: *Physics Reports* 405.5-6 (Jan. 2005), pp. 279–390. ISSN:
1139 0370-1573. doi: 10.1016/j.physrep.2004.08.031. URL: <http://dx.doi.org/10.1016/j.physrep.2004.08.031>.
- 1141 [53] HongSheng Zhao. “Analytical models for galactic nuclei”. In: *Mon. Not. Roy. Astron. Soc.*
1142 278 (1996), pp. 488–496. doi: 10.1093/mnras/278.2.488. arXiv: astro-ph/9509122
1143 [astro-ph].

- 1144 [54] H. C. Plummer. “On the Problem of Distribution in Globular Star Clusters: (Plate 8.)”
1145 In: *Monthly Notices of the Royal Astronomical Society* 71.5 (Mar. 1911), pp. 460–470.
1146 ISSN: 0035-8711. doi: [10.1093/mnras/71.5.460](https://doi.org/10.1093/mnras/71.5.460). eprint: <https://academic.oup.com/mnras/article-pdf/71/5/460/2937497/mnras71-0460.pdf>. URL:
1147 <https://doi.org/10.1093/mnras/71.5.460>.
- 1149 [55] Daniel R. Hunter. “Derivation of the anisotropy profile, constraints on the local velocity
1150 dispersion, and implications for direct detection”. In: *JCAP* 02 (2014), p. 023. doi:
1151 [10.1088/1475-7516/2014/02/023](https://doi.org/10.1088/1475-7516/2014/02/023). arXiv: [1311.0256 \[astro-ph.CO\]](https://arxiv.org/abs/1311.0256).
- 1152 [56] Barun Kumar Dhar and Liliya L. R. Williams. “Surface mass density of the Einasto family
1153 of dark matter haloes: are they Sersic-like?” In: *Mon. Not. Roy. Astron. Soc.* (2010). doi:
1154 [10.1111/j.1365-2966.2010.16446.x](https://doi.org/10.1111/j.1365-2966.2010.16446.x).
- 1155 [57] M. Baes and E. Van Hese. “Dynamical models with a general anisotropy profile”. In: *Astron. Astrophys.* 471 (2007), p. 419. doi: [10.1051/0004-6361:20077672](https://doi.org/10.1051/0004-6361:20077672). arXiv:
1156 [0705.4109 \[astro-ph\]](https://arxiv.org/abs/0705.4109).
- 1158 [58] Matthew G. Walker, Edward W. Olszewski, and Mario Mateo. “Bayesian analysis of re-
1159 solved stellar spectra: application to MMT/Hectochelle observations of the Draco dwarf
1160 spheroidal”. In: *mnras* 448.3 (Apr. 2015), pp. 2717–2732. doi: [10.1093/mnras/stv099](https://doi.org/10.1093/mnras/stv099).
1161 arXiv: [1503.02589 \[astro-ph.GA\]](https://arxiv.org/abs/1503.02589).